National Library of Canada
Bibliothèque nationale du Canada

Canadian Theses Service
Service des thèses canadiennes

Ottawa, Canada
K1A 0N4

NOTICE

The quality of this microform is heavily dependent upon the quality of the original thesis submitted for microfilming. Every effort has been made to ensure the highest quality of reproduction possible.

If pages are missing, contact the university which granted the degree.

Some pages may have indistinct print especially if the original pages were typed with a poor typewriter ribbon or if the university sent us an inferior photocopy.

Previously copyrighted materials (journal articles, published tests, etc.) are not filmed.

Reproduction in full or in part of this microform is governed by the Canadian Copyright Act, R.S.C. 1970, c. C-30.

AVIS

La qualité de cette microforme dépend grandement de la qualité de la thèse soumise au microfilmage. Nous avons tout fait pour assurer une qualité supérieure de reproduction.

S'il manque des pages, veuillez communiquer avec l'université qui a conféré le grade.

La qualité d'impression de certaines pages peut laisser à désirer, surtout si les pages originales ont été dactylographiées à l'aide d'un ruban usé ou si l'université nous a fait parvenir une photocopie de qualité inférieure.

Les documents qui font déjà l'objet d'un droit d'auteur (articles de revue, tests publiés, etc.) ne sont pas microfilmés.

La reproduction, même partielle, de cette microforme est soumise à la Loi canadienne sur le droit d'auteur, SRC 1970, c. C-30.

NL-339 (r. 88/04)

Canada

THE UNIVERSITY OF ALBERTA

ENCAPSULATION AS A METHOD FOR CONTROLLING RADIATION DAMAGE IN THE ELECTRON MICROSCOPE

by

PHILIP M. RICE

A THESIS

SUBMITTED TO THE FACULTY OF GRADUATE STUDIES AND RESEARCH

IN PARTIAL FULFILMENT OF THE REQUIREMENTS FOR THE DEGREE

OF MASTER OF SCIENCE

IN

SOLID STATE PHYSICS

DEPARTMENT OF PHYSICS

EDMONTON, ALBERTA

SPRING 1988

Permission has been granted to the National Library of Canada to microfilm this thesis and to lend or sell copies of the film.

The author (copyright owner) has reserved other publication rights, and neither the thesis nor extensive extracts from it may be printed or otherwise reproduced without his/her written permission.

L'autorisation a été accordée à la Bibliothèque nationale du Canada de microfilmer cette thèse et de prêter ou de vendre des exemplaires du film.

L'auteur (titulaire du droit d'auteur) se réserve les autres droits de publication; ni la thèse ni de longs extraits de celle-ci ne doivent être imprimés ou autrement reproduits sans son autorisation écrite.

ISBN 0-315-42736-1

THE UNIVERSITY OF ALBERTA

RELEASE FORM

NAME OF AUTHOR PHILIP M. RICE

TITLE OF THESIS ENCAPSULATION AS A METHOD FOR CONTROLLING RADIATION DAMAGE IN THE ELECTRON MICROSCOPE

DEGREE FOR WHICH THESIS WAS PRESENTED MASTER OF SCIENCE

YEAR THIS DEGREE GRANTED SPRING 1988

Permission is hereby granted to THE UNIVERSITY OF ALBERTA LIBRARY to reproduce single copies of this thesis and to lend or sell such copies for private, scholarly or scientific research purposes only.

The author reserves other publication rights, and neither the thesis nor extensive extracts from it may be printed or otherwise reproduced without the author's written permission.

(SIGNED) Philip Rice

PERMANENT ADDRESS:
RR#3
Ilderton, Ont.
Canada N0M 2A0

DATED December 8 1987

THE UNIVERSITY OF ALBERTA

FACULTY OF GRADUATE STUDIES AND RESEARCH

The undersigned certify that they have read, and recommend to the Faculty of Graduate Studies and Research, for acceptance, a thesis entitled ENCAPSULATION AS A METHOD FOR CONTROLLING RADIATION DAMAGE IN THE ELECTRON MICROSCOPE submitted by PHILIP M. RICE in partial fulfilment of the requirements for the degree of MASTER OF SCIENCE.

.....

Supervisor

.....

.....

Date.....Dec. 8, 1987.....

Abstract

This paper describes a study of a fairly new and relatively untried method for controlling radiation damage in the electron microscope. The method, called encapsulation, uses surface coatings to reduce the radiation sensitivity of the samples. The study was predominantly based on EELS, which was used to quantify the chemical damage (mass loss), but also included electron diffraction to monitor structural damage. Encapsulation was tested on several radiation-sensitive materials whose damage mechanisms are fairly well understood. Samples of an organic crystal and two alkali halides were especially prepared to allow quantitative comparisons of radiation sensitivity between encapsulated and unencapsulated portions of the same specimen. The proposed protection mechanisms for both material groups are discussed. A brief review of EELS is also contained in this paper to help introduce the technique to those who are unfamiliar with it, and to help stress its many uses.

The evidence presented in this paper shows that encapsulation is indeed a viable method for controlling radiation damage in the electron microscope.

Acknowledgement

I wish to express my gratitude to DR. R. F. Egerton, my supervisor, for his encouragement and help during this project. I would also like to thank Dr. P. A. Crozier for his guidance and patience throughout this study.

I am indebted to the Department of Physics for the awarding of a teaching assistantship, and to the members of my supervisory committee for reading my thesis.

Finally, I wish to thank my loving parents, without whom none of this would be possible.

Table of Contents

Page

1. INTRODUCTION TO RADIATION DAMAGE... 1

1.1 RADIATION DAMAGE AND ITS IMPORTANCE... 1

1.2 DAMAGE MECHANISMS... 3

1.3 METHODS FOR MONITORING RADIATION DAMAGE 7

1.3.1 STRUCTURAL DAMAGE TO CRYSTALLINE SPECIMENS 7

1.3.2 MASS LOSS (CHEMICAL DAMAGE) 9

1.4 CONTROLLING RADIATION DAMAGE 12

1.4.1 PROVEN METHODS 12

1.4.2 ENCAPSULATION 13

2. INSTRUMENTATION 16

2.1 INTRODUCTION 16

2.2 JEOL JEM-100B ELECTRON MICROSCOPE 18

2.3 MAGNETIC-PRISM SPECTROMETER 22

2.3.1 GENERAL SPECTROMETER CONSIDERATIONS ... 22

2.3.2 COUPLING TO THE MICROSCOPE... 28

2.4 SERIAL DETECTION AND COUNTING SYSTEM 30

2.5 EVAPORATION SYSTEM... 34

3. INTERPRETATION AND QUANTIFICATION OF ENERGY-LOSS SPECTRA... 37

3.1 INTRODUCTION 37

TABLE OF CONTENTS CONTINUED

PAGE

3.2 INTERPRETING ENERGY-LOSS SPECTRA IN TERMS OF SCATTERING 39
3.2.1 ZERO-LOSS REGION... 39
3.2.2 LOW-LOSS REGION... 41
3.2.3 HIGH-LOSS REGION 44
3.3 QUANTIFICATION OF INNER-SHELL EDGES... 48
3.3.1 THE ANGULAR AND ENERGY-LOSS DISTRIBUTION OF INNER-SHELL SCATTERING... 48
3.3.2 PARTIALLY INTEGRATED IONIZATION CROSS SECTION 51
3.4 ANALYSIS PROCEDURE... 54

4. ENCAPSULATION EXPERIMENTS.... 58
4.1 INTRODUCTION... 58
4.2 SPECIMEN PREPARATION... 59
4.3 CLCUPC 65
4.3.1 EXPERIMENTAL PROCEDURE... 65
4.3.2 RESULTS AND DISCUSSION 68
4.3.3 CONCLUSION 78
4.4 ALKALI HALIDES... 79
4.4.1 EXPERIMENTAL PROCEDURE... 79
4.4.2 RESULTS AND DISCUSSION... 81
4.4.3 CONCLUSION... 94

TABLE OF CONTENTS CONTINUED

PAGE

5. CONCLUDING STATEMENTS AND
SUGGESTIONS FOR FURTHER STUDY 96

REFERENCES... 99

APPENDIX A... 106

List of Figures

Figure		Page
1.1	Conceptual drawing of the atom displacment mechanisms in alkali halides	5
2.1	Typical EELS system	17
2.2	Column cross section of JEM-100B Electron Microscope	19
2.3	The focusing and dispersive properties of a magnetic prism	23
2.4	The cross section of Gatan Electron Energy-Loss Spectrometer, Model 607	26
2.5	The effect of the compensation circuit on the appearance of the zero loss peak as seen in a slow scan and with a narrow slit	27
2.6	Two configurational couplings of the CTEM to the spectrometer	29
2.7	A typical serial-acquisition system for energy-loss spectroscopy	31
2.8	A typical vacuum system	35
3.1	A sketch of a typical energy loss spectrum	38
3.2	The angular distributions of the scattered electrons	40

3.3 Squence of energy loss spectra of NaCl after increments of dose have been recieved in the region under examination 43

3.4 Bethe surface for K-shell ionization, calculated using a hydrogenic model 50

3.5 Partial cross section for K-shell ionization of second period elements 53

3.6 Two-area method of background fitting 55

4.1 A partially-encapsulated specimen 61

4.2 The molecular structure of pentadecachlorinated copper phthalocyanine 63

4.3 Typical diffraction patterns of damaged and undamaged ClCuPc 69

4.4 Typical electron energy-loss spectra of damaged and undamaged ClCuPc 71

4.5 Areal density N^{Cl} of chlorine in ClCuPc as a function of exposure to 80keV electrons 72

4.6 Examples of single crystal and polycrystalline structure 75

4.7 Typical energy-loss spectra of damaged and undamaged LiF 82

4.8 Typical energy-loss spectra of damaged and undamaged CaF_2 83

4.9 Measured areal densities N in LiF, as a function of exposure to 80keV electrons 84

4.10 Measured areal densities N in CaF_2, as a function of exposure to 80keV electrons 86

4.11 Typical diffraction patterns observed during the experiments 88

4.12 Transmission electron micrograph displaying both damaged and undamaged specimen 90

4.13 Measured areal density of carbon N^C, in the LiF sample, as a function of dose 91

A.1 Illustration of Bragg reflection for close-packed crystals 107

A.2 Schematic diagram of the formation of a diffraction pattern in the TEM, with effective camera length L 109

Chapter 1

Introduction to Radiation Damage

1.1) Radiation Damage and Its Importance

To conduct a study of a method of controlling (reducing) radiation damage in the electron microscope, it is necessary to first define just what is meant by the term *radiation damage*. A rather vague, though valid, definition is the irreversible alteration of the atomic structure of a specimen caused by its interaction with the electron beam. This broad definition includes not only the permanent change in the position of atoms within the sample, called 'structural damage', but also the loss of any element from the irradiated volume, termed 'mass loss'.

Researchers have made use of radiation damage in the electron microscope for several years. The creation of ultra-fine holes for use as apertures (Muray et al 1983) and electron-beam lithography for the fabrication of micro-electronic circuitry (Mankiewich et al 1983, Muray et al 1984) are just some of the uses.

Generally, however, radiation damage is considered undesirable. Obviously any attempt at characterization of a specimen that results in the alteration or outright destruction of that sample, before sufficient information can be acquired, is self defeating. Radiation damage has always been of concern in analytical electron microscopy because it places a limit on the spatial resolution that can

be achieved in microanalysis (Egerton 1986). Certainly any attempt at determining the stoichiometry of a sample of unknown composition becomes suspect if the sample has suffered mass loss.

In recent years, controlling radiation damage has become even more important. With the advent of high-voltage microscopes (Mansfield et al 1987) and increased current densities used in high-resolution scanning transmission electron microscopes equipped with field emission sources (HR-STEM) (Thomas 1985, Berger et al 1987), an increasing number of materials are being classified as 'radiation-sensitive'. Thus it is important to find a method of controlling the damage which works for the majority of the specimens and microscopes.

1.2) Damage Mechanisms

The initial definition of radiation damage was necessarily vague, because the permanent perturbation of atomic structure may manifest itself in a material-dependent manner. In the case of biological and organic samples, the transfer of energy from the fast electrons (the interaction is called inelastic scattering) involves the excitation of valence electrons to higher energy states, may result in the scission (breakage) of bonds. This scission may create ions, free hydrogen, or halogens which (as volatile gases) may eventually leave the sample (Hobbs 1983), leaving behind residual molecules which may join with other damaged molecules to form new structure in the sample (polymerization and cross-linking) (Hobbs 1983). Such damage is an example of the loss of structural order accompanying mass loss. In the case of some organic crystalline samples, such as the chlorinated copper phthalocyanine (ClCuPc) studied in chapter 4, a sufficiently large dose can reduce the sample volume to an amorphous glass (Hobbs 1983).

For radiation-sensitive, inorganic crystalline samples, like the alkali halides, lithium fluoride (LiF) and calcium fluoride (CaF_2) (also studied in chapter 4), irradiation causes point defects which tend to accumulate to a rather high density. However, this high density of defects often does not alter the overall periodicity of the sample (Hobbs 1983). These point defects are often able to aggregate into

large structural deffects, such as dislocation loops and voids, which are visible in the electron microscope (Hobbs and Pascucci 1980, Chadderton et al 1976).

There are two accepted methods, one more dominant than the other, for the creation of point defects in alkali halides. Both damage mechanisms are displayed in figure 1.1. The process of minor concern is called 'knock-on' damage and it involves the transfer of momentum, from the fast electrons to the atomic nucleus, by direct Coulombic interaction (called elastic scattering)(Hobbs 1983). If sufficient momentum is transferred, the atom may be moved (knocked) from its lattice position. This creates two point defects: a vacancy (the empty lattice site) and an interstitial (the atom or ion no longer in its proper lattice site). If the damage occurs at the surface, it can be responsible for mass loss (Thomas 1985). Due to directionality of the momentum transfer, the sputtering (ejection of atoms) is likely to be from the surface through which the electrons leave the specimen (Hobbs 1983). For the experiments discussed in this thesis, knock-on damage is not likely to be the major damage mechanism because of the relatively small cross section for an incident electron energy of 80keV (Hobbs 1983).

The dominant damage mechanism for alkali halides falls under the heading of 'radiolysis', the indirect process which involves the interaction of a fast electron with

(a) Knock-on (b) Radiolysis

Fig 1.1) Conceptual drawings of the atomic displacment mechanisms in alkali halides.

an atomic electron. In this case the interaction generates a localized exciton state with a lifetime greater than an atomic vibration period of ~1 ps (Hobbs 1983). The exciton state decays via the Pooley-Hersh mechanism, which involves the mechanical relaxation of surrounding ion cores. This process results in a halogen vacancy with a trapped electron (F centre) and a crowdion interstitial (H centre, made up of four halogen atoms sharing three lattice sites or two sharing one site) (Kabler and Williams 1978). An F and an H centre make up what is called a Frenkel pair, and such defects may aggregate to form voids (collection of F centres) or precipitates (collection of H centres) (Chadderton et al 1976, Hobbs 1979).

There is evidence which suggests that H centres may reach the surface of the crystal, either by diffusion or a momentum transfer process called a 'focussed replacement sequence', where they can be released (sputtered) from the sample (Townsend and Lama 1983). This selective mass loss of halogen atoms was the focus of the encapsulation experiments (described in chapter 4) performed on the alkali halides.

1.3) Methods for Monitoring Radiation Damage

Methods for determining the extent to which damage, caused by the electron beam, has altered the sample area under investigation have increased in sophistication over the years. Methods such as weighing the specimen before and after irradiation (which required uncharacteristic microscope specimens) and measuring the change in the total scattering power of the sample, gave general information about mass loss but are rarely used now because of the availability of more advanced techniques. Advances in theory and improvements in instrumentation make it possible to study specific manifestations of radiation damage using the methods described in this section.

1.3.1) Structural Damage to Crystalline Specimens

'Structural damage', caused by interaction with the electron beam, encompasses not only local disruptions of the atomic structure (such as dislocations, fault planes and voids) but also the permanent phase transformation of a material (such as oxidation), as well as the complete loss of all crystal structure. There are a couple of methods which can monitor this damage on a fine scale. One is high-resolution electron microscopy (HREM); the other is electron diffraction.

HREM is the use of an electron microscope which has been optimized in terms of spatial resolution (Spence 1980). Structural damage can be manifested as the disappearance of fine lattice fringes (Hobbs 1983), the loss of contrast in the images, or even a visible change from molecular columns to an amorphous structure (Smith et al 1986). Acquiring images which can be analysed requires very precise control of the microscope and usually a special high-resolution pole-piece.

Electron diffraction can be performed in any electron microscope and was used as a monitor of structural damage for the experiments discussed in this thesis. Crystalline samples have periodic planes of atoms (or molecules) which reflect some of the incident electrons according to Bragg's law:

$$2d\sin\Theta = n\lambda \qquad 1.1$$

where d is the spacing of the atomic planes,
Θ is the angle of reflection,
n is the order number,
λ is the wavelength of the incident electrons.

This reflection results in spots (or in the case of polycrystalline samples, rings) whose intensity can be monitored. As structural damage increases, the extent of

atomic planes satisfying Bragg's law is reduced, and the intensity of the spots (rings) will be decreased. If the crystal simply exchanges its structure for another, as is often the case when a sample oxidizes, some spots fade and new ones appear. If, on the other hand, the sample is reduced to an amorphous glass, as occurs for most organic samples, the spots fade completely, leaving only a diffuse background intensity.

By monitoring the dose required to bring about such changes in the diffraction pattern, it is possible to determine, quantitatively, the radiation-sensitivity of various materials. (A more complete description of electron diffraction theory appears in appendix A.)

1.3.2) Mass Loss (Chemical Damage)

Radiation damage to the atomic structure is often accompanied by mass loss of light elements from the irradiated volume (Thomas 1985). This mass loss is a major problem for analytical electron microscopy, because it introduces uncertainty into the stoichiometric elemental concentration values determined for radiation-sensitive materials. There are two techniques of monitoring mass loss which could be used to study the process. One of the methods is energy dispersive X-ray spectroscopy (EDX); another is electron energy-loss spectroscopy (EELS).

EDX uses the incident beam to excite atomic electrons from core levels to states above the Fermi level. An electron from a higher state will fall to fill the empty orbital, and may emit a characteristic X-ray in the process. The detector disperses the X-rays according to their energy and the spectrum displays characteristic peaks on a low background. The characteristic X-rays are emitted isotropically, and the collection efficiency of the detector is very low. However, this can be offset by the fact that the quantification procedure may be fairly simple (at least for thin films). The reduction in intensity of a particular elemental peak is related to the number of atoms, of that element, lost from the sample volume. A drawback to this procedure is that the very low X-ray fluorescence yield for elements with $Z < 11$ (which includes most of the elements of interest in a study of mass loss) results in a relatively poor sensitivity to the elements (Egerton 1986).

EELS uses a beam of monoenergetic electrons (energy= E_o) which, after undergoing interactions as they are transmitted through a thin specimen, are energy dispersed by means of a magnetic spectrometer. The spectrum contains the core-loss signals which appear as protruding edges on a large, falling background. (An energy-loss spectrum is displayed in chapter 3, in figure 3.1.) Because the scattering of the beam by the sample is forward peaked, the EELS system has a high collection efficiency, resulting in relatively high core-loss signals. The high dispersive

powers of the spectrometer (described in chapter 2) gives EELS its high energy resolution (Egerton 1986). Also, the quantification process (described in chapter 3) allows standardless, absolute values of elemental concentrations to be determined from the core-loss edges (Egerton 1982a). Since the core-loss edges, for the elements with Z>2, are easily recognizable by their energy thresholds, EELS is an excellent *in-situ* method of monitoring mass loss. For these reasons, EELS tends to have an advantage over EDX for monitoring of the light-element mass loss which occurs when radiation-sensitive specimens are irradiated. The majority of the radiation damage information discussed in chapter 4 was obtained using EELS.

1.4) Controlling Radiation Damage

The importance of reducing radiation damage to sensitive specimens has already been discussed in this chapter. This section will outline methods that can be employed to reduce the radiation damage. Besides encapsulation, which is studied in this thesis, there are two currently used techniques as discussed below.

1.4.1) Proven Methods

One widely used method of reducing the rate of damage in the electron microscope is termed 'cryogenics' (Hobbs 1983). This method involves the cooling of the sample, usually with liquid nitrogen (T~76K) while the microanalysis is conducted (Egerton 1982b). Values for the reduction in mass loss go as high as a factor of ~100 (Egerton 1982b). There is, however, evidence that the structural damage is not reduced by similar factors (Hobbs 1983). In fact, once the irradiated specimen is brought back up to room temperature, there is significant mass loss (Egerton 1980). Therefore, all microanalysis of an interesting area must be carried out once the specimen area has been irradiated. That requirement, and the fact that this method requires a special cold stage to maintain temperature stability, are both disadvantages of the cryogenic technique for controlling radiation damage.

Another widely used method is appropriately called the 'minimum-dose technique' (Hobbs 1983). The technique involves exposing a sample area of interest only while sufficient electron statistics are being acquired. Between subsequent acquisitions, and for the initial focusing, the beam is deflected onto a nearby region, which is not of interest. There are also a few disadvantages to this technique. First, the deflection of the beam requires additional instrumentation on the microscope. Secondly, if the minimum dose required by the detector is larger than the dose required to damage the sample, the technique is ineffective.

1.4.2) Encapsulation

The method for controlling radiation damage, studied in this thesis, is called encapsulation. It involves evaporating surface coatings onto the radiation-sensitive material. Since samples are often prepared with a thin carbon layer on the bottom (for support), the only addition is a thin layer on the top surface. This method requires no additional instrumentation for the microscope and can be used with most specimens.

The original study of encapsulation used conducting layers of gold and aluminium. Taking as damage criterion the fading of the diffraction pattern, it was found that a reduction in the damage rate by factors of 3 to 5 were

obtained (Salih and Cosslett 1974). These authors explained the effect of their surface coatings in terms of the conducting layer stopping the creation of strong local electric fields. Later experiments, by Fryer and Holland (1983) and Fryer (1984), showed similar protection factors using carbon and SiO layers. Since SiO is an insulator, not a conductor, the original explanation for the encapsulation effect becomes suspect. Fryer expressed the belief that an increased recombination rate, due to the reduction in the out-flux of freed atoms, was the reason for the effectiveness of the encapsulation layer (Fryer 1984).

All of these earlier studies were conducted on organic, single crystal samples and concerned themselves with structural damage only. Thus one of the dominant reasons for undertaking this encapsulation study, from an EELS perspective, was to quantify the effectiveness of the surface coatings at reducing mass loss. With the hope of gaining a greater understanding of the mechanism by which the encapsulation layer affects the radiation-sensitivity of the sample material, chlorinated copper phthalocyanine (ClCuPc) was chosen as one of the sample materials. ClCuPc was one of the organic crystalline materials on which the encapsulation had been shown to have a strong positive effect (Fryer 1984). It was also sufficiently radiation resistant to allow accurate EELS analysis to be perfomed over a prolonged exposure. Another aim of this study was to extend the list of materials on which encapsulation had been

tested. Since the damage mechanisms for the alkali halides are fairly well understood, LiF and CaF_2 were also chosen as test samples.

Carbon was chosen as the encapsulation material for several reasons. It had already been proven as an effective encapsulation material by Fryer and Holland (1983). Moreover, carbon does not oxidize in air, and its low scattering power does not greatly increase the background intensity of the electron energy-loss spectrum. It is also worth mentioning that carbon can easily be prepared as an amorphous layer, therby minimizing additional fine structure which could interfere with electron microscope imaging.

Chapter 2

Instrumentation

2.1) Introduction

The instrumentation used for the study of radiation damage in the electron microscope is displayed in a conceptual diagram in figure 2.1 . Portions marked one through three are contained in the electron microscope which belongs to the Electron Microscopy Group at the University of Alberta, and is described in section 2.2 . For the EELS experiments, it was necessary to energy-analyse the transmitted electrons (Egerton 1980b). This was acomplished with the use of a commercially available magnetic spectrometer described in section 2.3 . The pre-spectrometer lenses in the electron microscope were used to couple the microscope to the spectrometer in two configurations which are also described in section 2.3 . The final requirements for the EELS experiments included the detection, counting, and storage of the energy-loss spectra. The components of this system used in the experiments are described in section 2.4 . The evaporation system employed to prepare the partially-encapsulated radiation-sensitive specimens is described in section 2.5 .

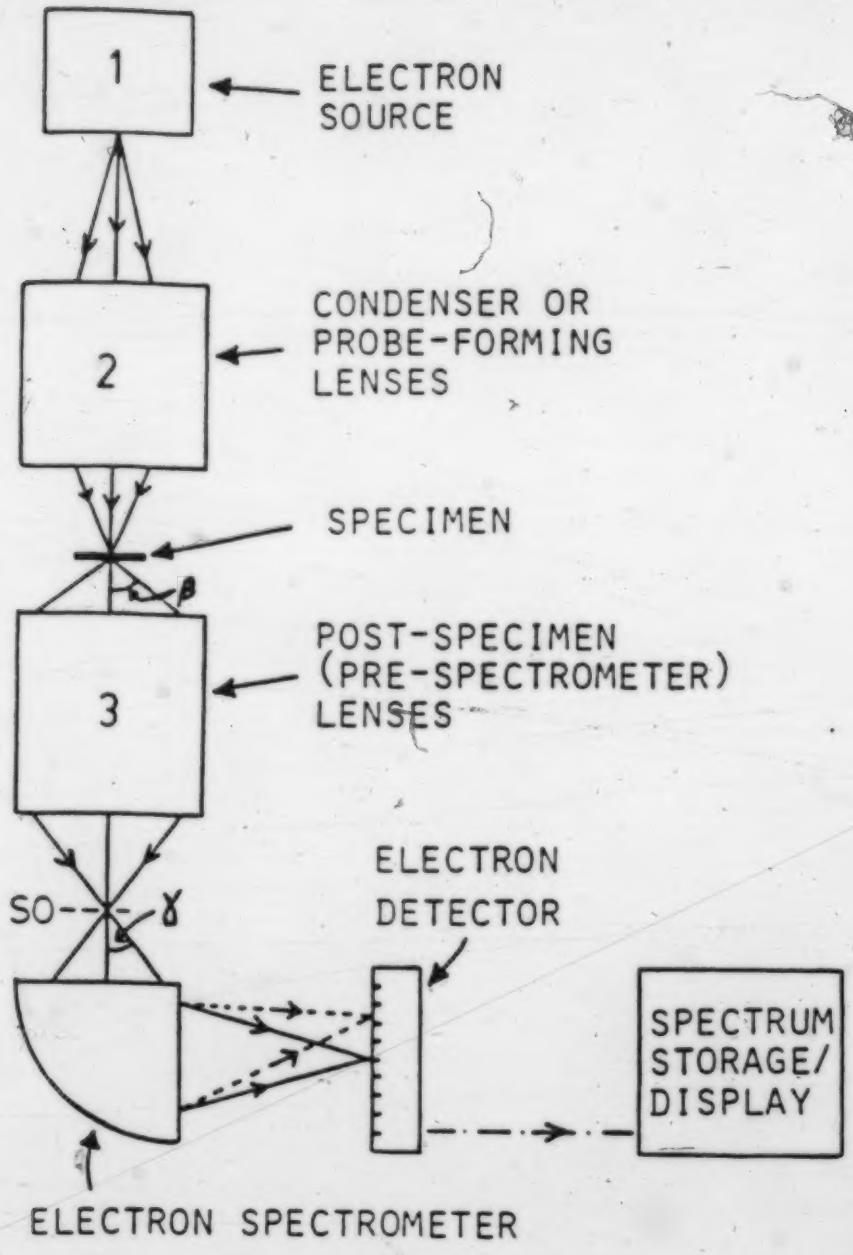

Fig 2.1) Typical EELS system (Egerton 1982a).

2.2) JEOL JEM-100B Electron Microscope

All the radiation damage experiments discussed in this thesis were conducted with the use of a JEOL JEM-100B electron microscope. A diagram of the conventional transmission electron microscope (CTEM) is shown in figure 2.2 . The electron gun sits at the top of the column and consists of a heated tungsten filament surrounded by a negatively charged Wehnelt cylinder. It is the controllable difference in potential (20kV to 100kV) between the filament and the grounded anode plate (which sits several cm below) that provides the acceleration for the electron beam. All experiments discussed in this thesis used electrons of incident energy E_o= 80keV.

Once the beam has been formed and accelerated, it enters the two condenser lenses. These lenses give the operator control over the beam's angular spread and its size (beam diameter), while ensuring that there is sufficient intensity at the specimen. Below the condenser lenses is a condenser aperture which is used to further limit the beam's angular spread, and thus helps to reduce the lens aberrations.

The electron beam next encounters the specimen which must be thin enough to permit the beam to be transmitted through with sufficient intensity. The interactions of the beam with the specimen are discussed in the next chapter.

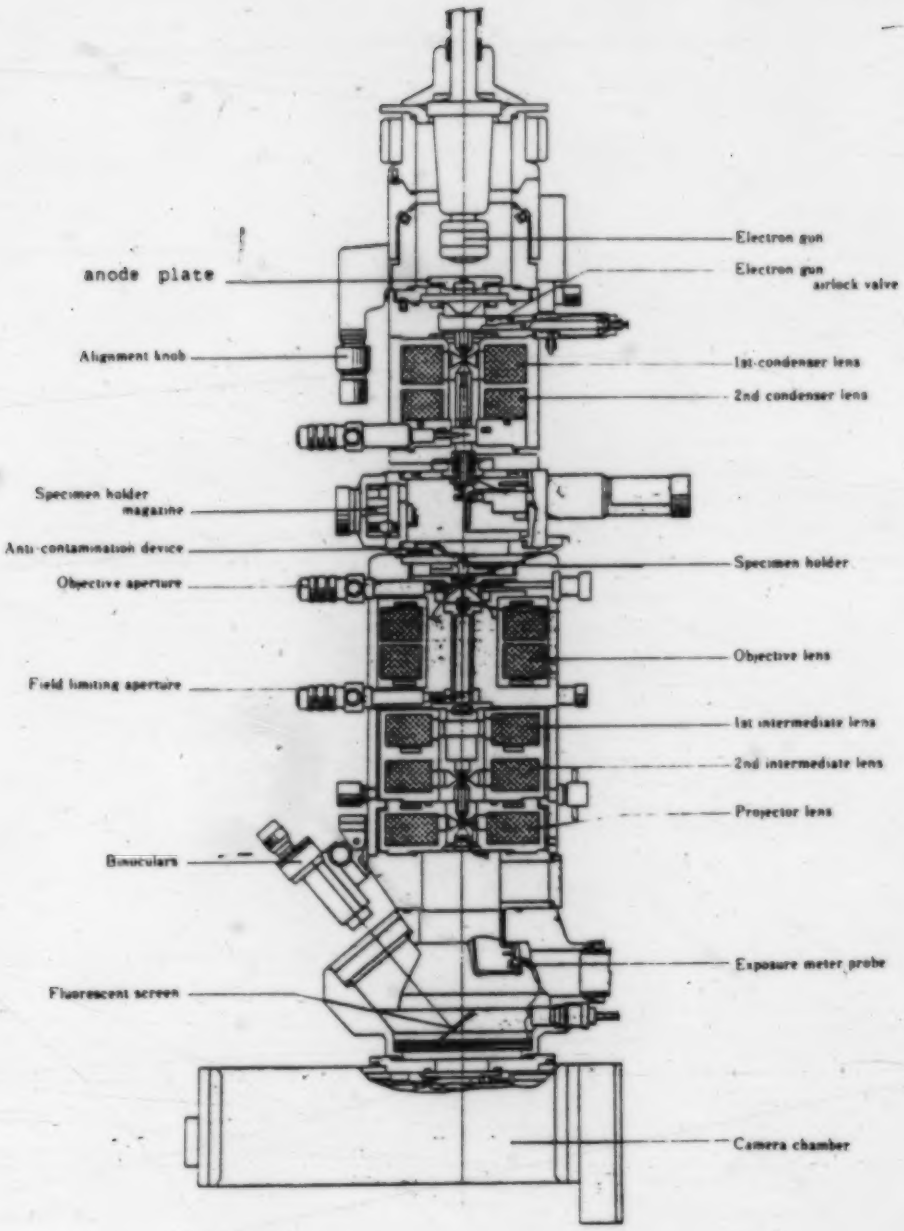

Fig 2.2 Column cross section of JEM-100B Electron Microscope.

Following the specimen is the objective lens whose object plane is the bottom surface of the specimen. It is the objective lens' job to produce a true and accurate point for point image of the specimen. Any defect in that image will be propagated by the lenses which follow. Thus the objective is the most important lens in the electron microscope.

In the back-focal plane of the objective lens (which contains the diffraction pattern of the specimen) there is an objective aperture of variable size. Electrons which have been scattered beyond a certain angle β strike the aperture and are removed from the transmitted beam. It is this aperture which is largely responsible for contrast in the image. It also helps to limit the spherical aberration of the objective lens.

In the image plane of the objective lens there is another aperture called the field limiting (or selected area) aperture. This variable aperture is used to select an area of the image (actually the electrons from a particular area of the specimen) from which the operator wishes to view the diffraction pattern. This aperture can also be used to restrict the electron intensity reaching the spectrometer.

The intermediate lenses and the projector lens, each of which use the image plane of the previous lens as their object plane, simply magnify the image created by the objective lens. The image is projected onto either the fluorescent screen at the base of the column, the

photographic plate just below the screen, or the entrance to the spectrometer which is mounted just below the camera chamber.

Between the bottom of the specimen and the objective aperture, there was an anti-contamination device which was kept at liquid nitrogen temperature throughout the experiments. Since the ambient vacuum pressure within the column was typically 2×10^{-6} torr, this device was essential in reducing the rate at which a carbon contamination layer built up on the irradiated portion of the specimen.

2.3) Magnetic-Prism Spectrometer

2.3.1) General Spectrometer Considerations (Including The Gatan 607 Magnetic Prism Spectrometer)

In order to study the effect the irradiation had on the samples, it was necessary to energy analyse the transmitted beam of electrons. It is obvious that electrons with different kinetic energies will have different velocities. This fact is exploited by having the electrons enter a magnetic field, B, which is perpendicular to the electrons' direction of motion. The resultant radius of curvature of the electrons' trajectory, R, is dependent on their velocity v as defined by equation 2.1 .

$$R = \left(\frac{\gamma m_o}{eB}\right) v \qquad 2.1$$

where $\gamma = (1-v^2/c^2)^{-1/2}$ a relativistic factor

c = the speed of light

m_o = electron rest mass

e = electron charge

The characteristic angle of deflection, Φ, for convenience is often made to be 90°, as shown in figure 2.3(a). As equation 2.1 shows, the greater the energy loss (i.e. the lower the energy and velocity) the smaller is R, which translates into an increase in the value of Φ (see the dashed lines in fig. 2.3). The typical dispersion of a magnetic-prism spectrometer is on the order of 2 μm/ev .

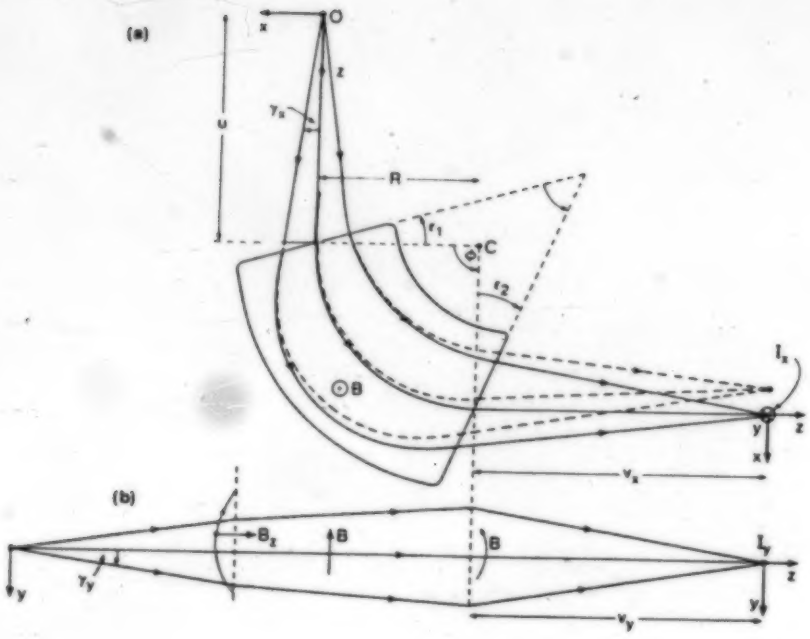

Fig 2.3) The focusing and dispersive properties of a magnetic prism. The coordinate system rotates with the electrons, so the z-axis is always the direction of motion of the central, zero-loss trajectory (optic axis). The dashed lines represent the trajectory of electrons which have lost energy.

(a) Shows the radial focusing in the x-z plane.

(b) Shows the axial focusing in the y-z plane.

This type of magnet is called a 'prism' because its effect on electrons is analogous to that of an optical prism's effect on white light.

The magnetic spectrometer must do more than just bend and energy disperse the electrons. It is necessary for the spectrometer to focus the electrons of the same energy, regardless of their angular distribution as they enter the magnetic field, onto a point in the spectrometer image plane. To explain the focusing we can adopt the coordinate system notation as shown in fig 2.3 (see for example Egerton 1986). In this system, the y axis is antiparallel to the direction of the magnetic field. The z axis always represents the direction of motion of an electron following a central trajectory (the optic axis). The x axis stays perpendicular to both the y and z axis, and rotates about the y axis through an angle Φ to stay radial to the optic axis. Using this coordinate system, the focusing in the x direction is due to the different distances which electrons travel in the magnetic field (Egerton 1986). If the object is a sharp point O, then an electron that enters the spectrometer with a negative angle γ_x travels a shorter distance in the magnetic field than those that follow the central axis. As a result it is deflected through a smaller angle and will eventually cross the optic axis. An electron which enters the spectrometer with a positive angle γ_x travels a greater distance in the magnetic field than the electrons which follow the central axis, and is thus

deflected back toward the optic axis. It will cross the optic axis at the same position the negative x-value electrons do, and this point, I_x, is on the spectrometer image plane.

The focussing in the y direction, as shown in figure 2.3(b), is accomplished by careful design of the entrance and exit pole-pieces of the magnet. The trick is to arrange the focus so that the image distances v_x and v_y are equal, and thus I_x and I_y are the same point. The Gatan 607 (see figure 2.4) is such a spectrometer and it is is said to have a 'doubly-focused' magnet.

Since the design of the entrance and exit pole-pieces (actually setting the polepiece-tilt angles ϵ_1 and ϵ_2) must also remove second order aberrations, the actual theoretical considerations are quite complicated. The usual design has a convex entrance and a concave exit with appropriately shaped soft-magnetic mirror plates at either end to 'kill' the magnetic field outside of the spectrometer.

To aid in the aberration correction there are two external quadrupole and one sextupole device which can be controlled by the operator to help improve energy resolution. These devices are also used to allow the operator to change the position of the spectrometer object plane, so that a spectrometer may be coupled to any microscope.

It should also be mentioned that even when the utmost care is taken to shield the spectrometer from stray external

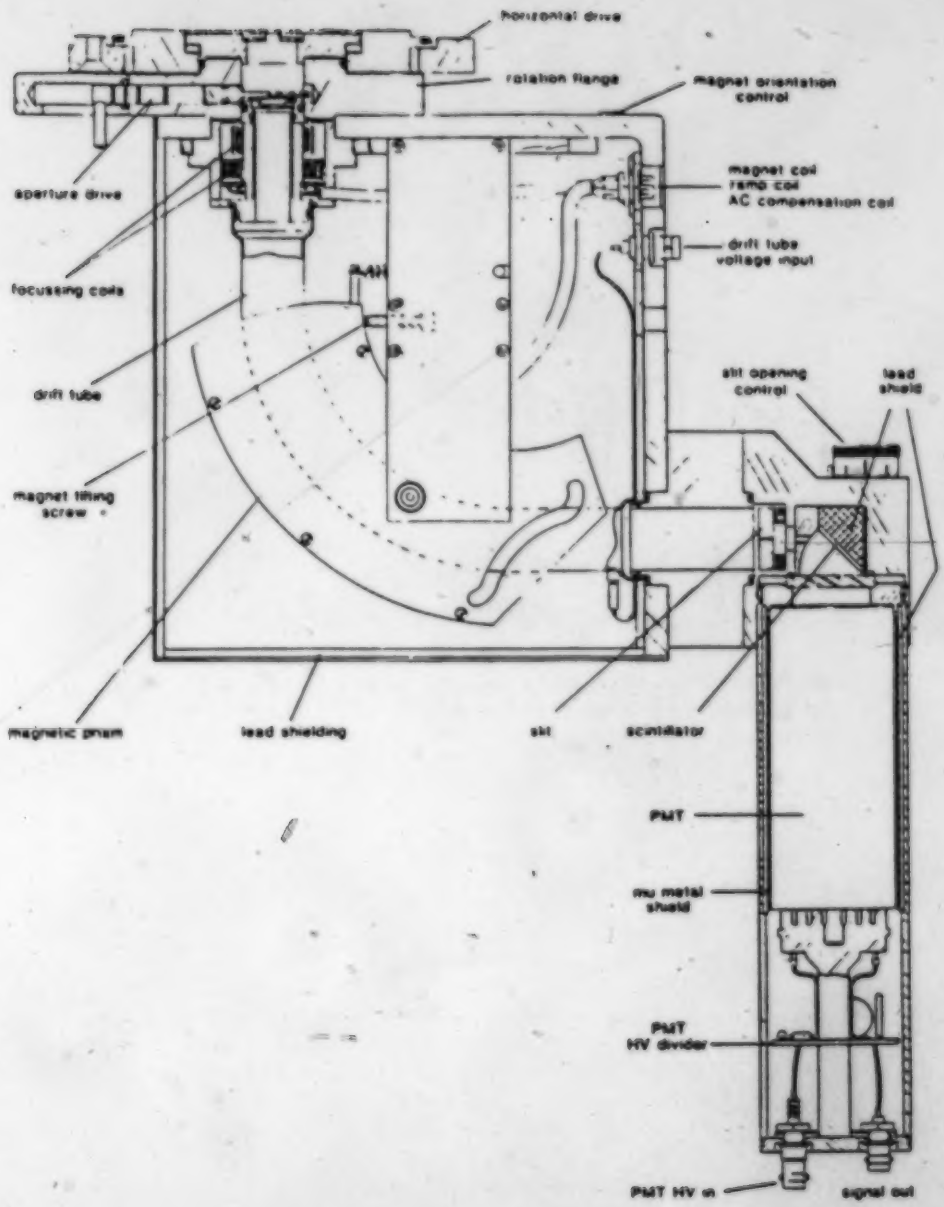

Fig 2.4) The cross-section of Gatan Electron Energy-Loss Spectrometer, Model 607.

fields (such as surrounding the spectrometer with mu-metal), their effects tend to remain evident in the energy-loss spectra. Since the major contribution to stray fields comes from mains-frequency fields, a circuit has been designed to compensate for their effect (Egerton 1982a). The circuit feeds a mains-frequency current of the correct phase and amplitude to the spectrometer scan coils so that the rippling is almost completely removed (see figure 2.5).

Uncompensated Compensated

Fig 2.5) The effect of the compensation circuit on the appearance of the zero loss peak as seen in a slow scan and with a narrow slit. (Gatan Inc.)

2.3.2) Coupling to the Microscope

To ensure that the energy-loss spectrum is not altered by image or diffraction information, the spectrometer object must be as small as possible. It is customary to focus the spectrometer so that the spectrometer object plane (SO) coincides with the back-focal plane of the projector lens in the CTEM. This allows the system to be used in two configurations (Egerton 1982a), both of which were used in the experiments discussed in chapter 4.

The first configuration is called 'diffraction coupling', and is shown in figure 2.6(a). When the CTEM is set up so that it displays the magnified image of the specimen on the screen (microscope image mode), then the spectrometer object is the diffraction pattern at the back-focal plane of the projector lens. This configuration allows the operator to take pictures of the image between successive energy-loss spectrum acquisitions. The collection semi-angle β is determined by the selection of the particular objective aperture size.

The other configuration is called 'image coupling' and is shown in figure 2.6(b). The CTEM is set up to display the diffraction pattern of the specimen on the screen (microscope diffraction mode), so the back-focal plane of the projector lens contains a low-magnification image of the specimen. The spectrometer is thus image coupled. The collection semi-angle β is determined by the spectrometer

entrance aperture (d=1,2,3,or5mm) and the intensity of the beam which enters the spectrometer can be controlled by appropriate choice of selected area aperture size. Image coupling allows the operator to monitor the diffraction pattern between successive energy-loss spectrum acquisitions.

(a) Diffraction Coupling (b) Image Coupling

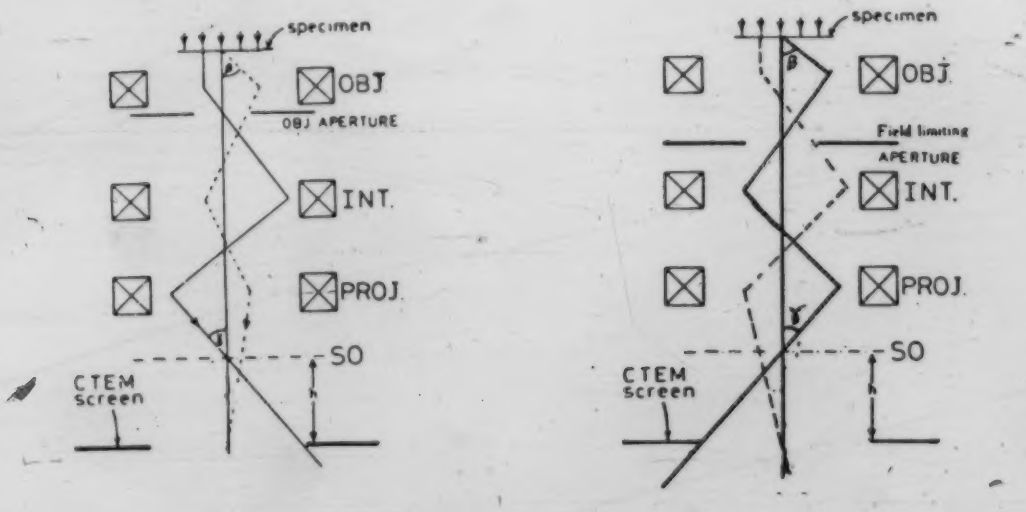

Fig 2.6) The coupling of the CTEM to the spectrometer whose object plane SO is at the back-focal plane of the projector lens. Both configurations were used in the experiments discussed in this thesis.

2.4)Serial Detection and Counting System

There are two different techniques for detecting an energy-loss spectrum. They are known as parallel detection and serial detection (Joy 1984). While a parallel detector is very efficient because it acquires the complete spectrum simultaneously, there was no parallel detector available for the experiments. All spectra reported in this thesis were serially acquired. The serial detection system is very inefficient because the spectrum is sampled sequentially. A slit of a few microns or less is used to sample the electrons in a narrow energy range. While there are a few artifacts introduced into the spectrum due to the detection system, the majority of these can be minimized, or corrected for, whenever they cause concern (Joy and Maher 1980).

A typical serial-acquisition system, as shown in figure 2.7, contains several major components (Egerton 1986). First, so that only the electrons of a particular energy-loss are detected at any given moment, a thin slit is place at the image plane of the spectrometer. Since the dispersive power of the magnet is only on the order of 2 μm/ev, the slit must be able to close to at least this value (2μm) for the cases in which energy resolution is the prime concern. For the case is which signal strength is a major factor, the slit must be able to open much wider to allow more signal to pass. The Gatan system used for aquiring the spectra for this study had a variable slit

width of 0 to 100 μm.

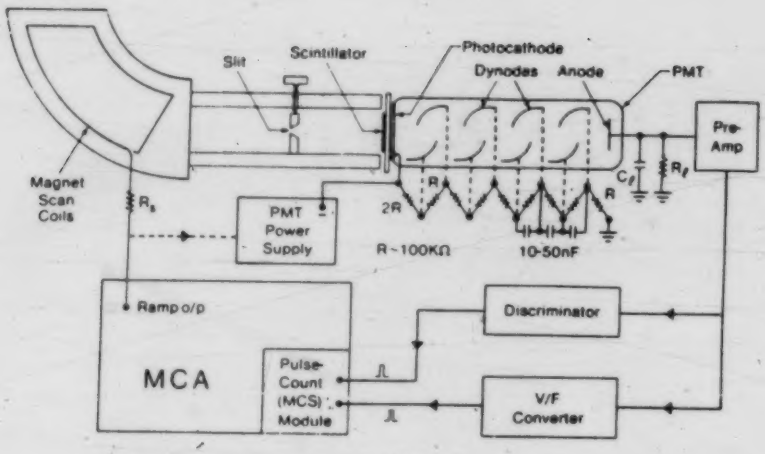

Fig 2.7) A typical serial-acquisition system for energy-loss spectroscopy.

Next in the system comes the detector which in our case was a scintillator followed by a photomultiplier tube (PMT). When an electron has passed through the energy-selecting slit it strikes the scintillator, and generates a large number of photons. The photons then strike the photocathode (at the top of the PMT), which absorbs the photons and emits electrons. These electrons strike the dynodes in the tube and each incident electron generates several secondary electrons that are accelerated and strike the next dynode. This cascading process results in a large number of electrons, typically 10^6, reaching the anode, at the base of the photomultiplier tube, for each of the incident photons. This 'pulse',when registered in the counting system, will be

representive of an electron of the proper energy having entered the detection system.

The next stage of the serial acquisition is the scanning of the spectrum across the slit in a linear manner. This can be accomplished by a couple of methods. The first case is for 'fast' scans, taken on the order of 60 Hz, which are often used while adjusting the analyser, and is acomplished by feeding a ramp current into pre or post-spectrometer 'dipole' coils. The other case is for normal scanning and uses separate windings on the main prism-magnet. The multichannel analyzer (MCA),which stores the spectrum one channel at a time, generates a channel advance pulse which can be used to generate a ramp current which is fed into the scan coils on the prism. The predicted non-linearity in the energy-loss axis, due to the changing magnetic field, is approximately .4% at E=1000ev, for E_0=100 keV (Egerton 1986).

The final step in the serial acquisition of an energy-loss spectrum is the conversion of the photomultiplier output into a value which can be stored in the MCA (which in this case was a Tracor Northern-1710). Due to the extensive dynamic range of the spectrum (10^7), the output from the PMT must be recorded in two separate counting modes.

For the Gatan system used in the experiments discussed in this thesis, when the incident electron arrival rate at the scintillator is less than 10^6 electrons/sec (1MHz), it

is possible to count, individually, the electron pulses as they leave the PMT (Disko 1986). This is called the pulse counting mode and is used for the high energy-loss region of the spectrum. To ensure that very little noise from the PMT enters the signal in this mode, there is usually a discriminator placed between the PMT and the MCA (actually the pulse counting module in the MCA), which only passes pulses of sufficient strength to have been generated by an electron entering the detector.

In the low-loss region of the spectrum, the electron arrival rate is too great and the pulse counting system no longer responds in a linear fashion. In this case the PMT's output becomes a continuous current or an average voltage. This voltage, which is directly proportional to the number of electrons striking the scintillator, is fed into a voltage controlled oscillator whose output is a continuous train of pulses which are counted in the same manner as the single-electron pulses by the MCA (Maher et al 1978). The frequency of pulses is linearly related to the electron intensity for a frequency $\leq$1.2 MHz (Cheng 1987),so all spectra were recorded at signal intensities that resulted in a frequency below this value.

The Gatan system allows for an automatic change in counting modes at a set channel. This change results in a jump or 'gain' in the spectrum between the low-loss and high-loss regions. The MCA acquires the spectrum, one channel at a time, over 1024 channels with a pre-set dwell

time for each channel. Once a complete spectrum was acquired, it was analysed with the help of a Texas Instruments Silent 700 data terminal and then stored using a TN-1117 floppy disk memory system.

2.5) Evaporation System

All the specimens studied in the experiments described in this thesis were prepared in an evaporation system, like that shown in figure 2.8 . The vacuum in the bell jar was created by combining two pumping methods. The rotary pump (S) was used to reduce the pressure to 5×10^{-2} torr. The oil-diffusion pump (N) was then used (backed by the rotary pump) to reduce the ambient vacuum pressure to 2×10^{-7} torr. A liquid nitrogen trap (L) was used to help freeze out condensable gases which might otherwise contaminate the samples.

To ensure uniform film thickness, the substrates (B) were placed approximately 14 cm above the evaporation sources (V), which were either Mo boats for the radiation-sensitive materials or graphite rods for the carbon evaporation. A shutter (E) was used to cover the substrates while outgassing the evaporation materials. It was also used to allow specimens of different thickness to be fabricated at the same time.

The approximate thickness of the evaporated film was monitored by a quartz-crystal microbalance (C), placed at

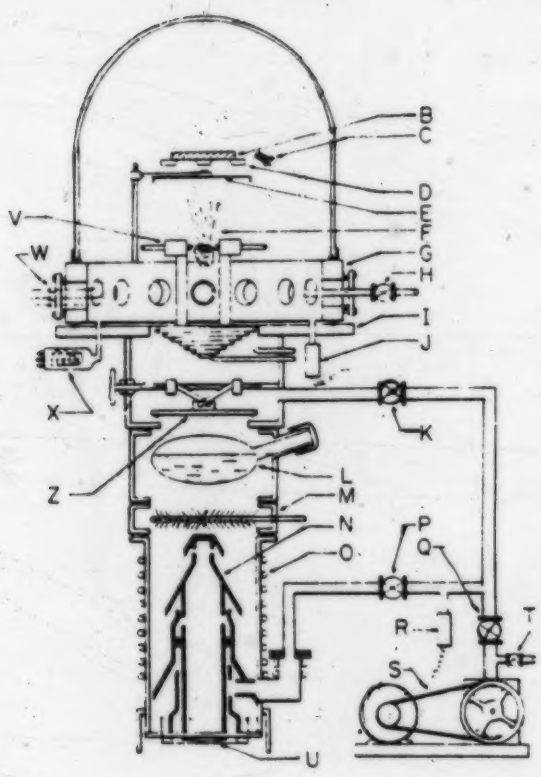

Fig 2.8) A typical vacuum system. The notation stand for B, substrate; C, quartzcrystal rate controller and deposition monitor; D, substrate mask; E, shutter; F, vapors from evaporation source; G, adapter collar between the bell jar and the pump baseplate flange; H, air-inlet valve; I, baseplate flange; J, Pirani or thermocouple gauge; K, roughing valve; L, liquid air trap; M, cooled chevron baffles; N, diffusion pump; O, cooling coils; P and Q, backing valves; R, Pirani gauge; S, forepump with air- inlet valve T; U, diffusion pump heater; V, filament holders; W, multiple feedthrough; X, ionization gauge;
Z, baffle valve.

the same height as the substrates. Gold coated crystals were used in the microbalance, whose calibration curve had already been calculated by Munoz (1983). The approximate thickness, t, of the film is given by equation 2.2 .

$$t = 1.7 \frac{\Delta f}{\rho} \qquad 2.2$$

where Δf is the change in the frequency of the quartz-crystal oscillator

ρ is the (bulk) density of the evaporated material

The absolute thickness of each layer of the specimen was later determined by an EELS method which will be described, along with the specimen preparation, in chapter 4.

Chapter 3

Interpretation and Quantification of Energy-Loss Spectra

3.1) Introduction

When a beam of electrons of energy E_0 is incident on a sample, the electrons are scattered by the atoms of the solid. The transmitted electrons will have a distribution in both angle, θ, and energy, E^*. The sample must be sufficiently thin ($t \leq$ a few hundred nm) so that this distribution is representitive of a single scattering profile. The difference between the initial energy and the energy of the transmitted electron is called the energy loss E, ($E=E_0 - E^*$). The distribution of intensity of the transmitted electrons as a function of their energy-loss is known as an energy-loss spectrum, an example of which is shown in figure 3.1 . The technique of studying materials by examining this distribution is known as electron energy-loss spectroscopy (EELS).

EELS can be used as an in-situ method for studying mass loss from material. The same electrons that cause the damage to the sample may be used in quantifying that damage. The majority of the radiation damage information presented in this thesis was ascertained by EELS, or more specifically, by studying the integrated intensity of the inner-shell ionization edges which appear in the spectra.

This chapter will describe the interpretation of an energy-loss spectrum and explain the quantification procedure.

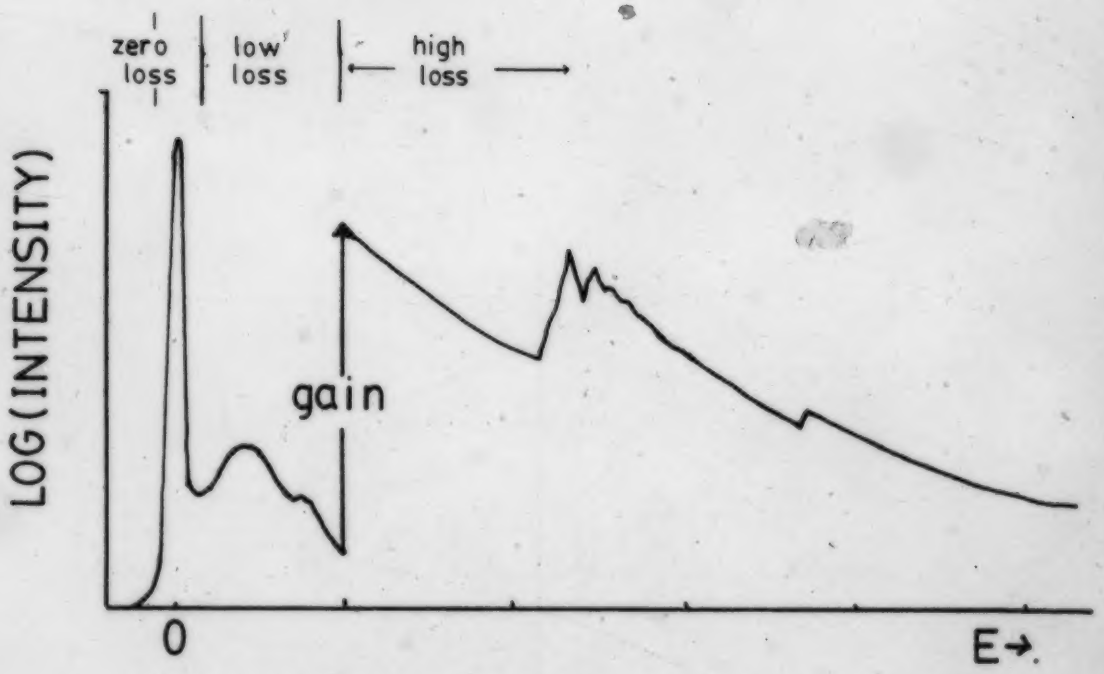

Fig 3.1) A sketch of a typical energy-loss spectrum. The three distinct regions are marked.

3.2) Interpreting Energy-Loss Spectra in Terms of Scattering

The energy-loss spectrum can be divided into characteristic regions, each with its own distinctive intensity distribution. With the proper analysis, each region can be made to yield information about the sample. An essential prerequisite to interpreting any part of an energy-loss spectrum is an understanding of the nature of the interactions between the beam and the sample, which give rise to the distribution in the first place. This section will consider each of the three regions individually and discuss the interactions that contribute to the electron intensity. Methods of extracting the information from each region will also be described.

3.2.1) Zero-Loss Region

The first 2 to 3 eV region of the spectrum contains the greatest intensity (for thin samples) but the least information of all three sections. The sole characteristic of the zero-loss region is a very sharp peak arising from electrons which have lost no energy, or an energy less than the resolution of the detection system. Unscattered electrons, that is electrons which have not interacted with the sample, have obviously lost no energy and contribute to this peak. Due to their lack of interaction, they can not offer any detailed information about the sample. The other major contribution to the region arises from electrons which

have been elastically scattered and lose very little energy but do have a rather broad angular distribution, as shown in figure 3.2 . Elastic scattering occurs when the incident electron interacts with the electrostatic field of the atom. If the electron passes close enough to the nucleus, it is deflected by its Coulomb attraction to the nuclear charge, but, due to the large difference in mass, the magnitude of the energy transfer is negligible.

Fig 3.2) The angular distribution of
(a) the incident beam
and unscattered electrons,

(b) elastically scattered electrons,

(c) plasmon excitations,

(d) inner-shell losses.

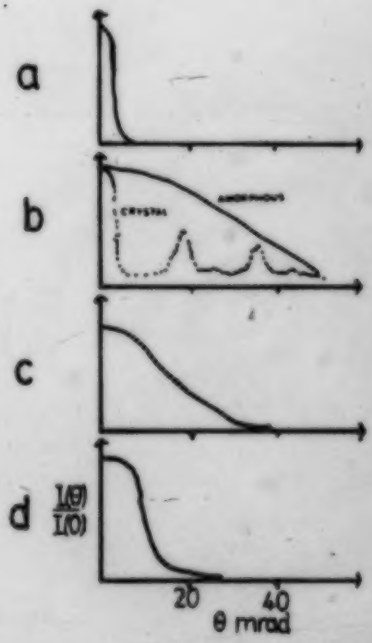

If the sample is a crystal (or polycrystalline) , the angular distribution of the elastically scattered electron intensity, studied using electron diffraction techniques, does contain a great deal of information about the crystal structure. However, like the unscattered electrons, the

elastically scattered electrons do not contain much information that can be determined using EELS.

For thicker specimens, elastic scattering becomes important because the inelastically scattered electrons, which do carry a great deal of EELS' information, have a higher probability of also being elastically scattered. Due to the large angular distribution of elastic scattering, this often removes these inelastically scattered electrons beyond the collection angle of the spectrometer and thus reduces the collection efficiency of the system.

There is another, less important, group of contributors to the zero-loss peak. They are the electrons which have undergone an interaction known as quasi-elastic. That is, the incident electron interacts with, or generates, a phonon in a crystal. 'Phonon' is the name given to the quanta of energy stored in a lattice vibration. The energy lost in generating a phonon is at maximum a tenth of an ev. Since the typical energy spread of a thermionic tungsten filament electron source is 1.5 eV and of a field-emission gun is .3 eV, it is extremely difficult for the detection system to distinguish the quasi-elastically scattered electrons from the elastically scattered ones.

3.2.2) Low-Loss Region

The next region, which runs from the edge of the zero loss peak (approx 5 eV) out to about 100 eV and is

characterized by at least one (usually broad) peak, is called the low-loss region. This low loss peak, which in the case of a conductor is called a 'plasmon peak', is due to the excitation of a number of loosely bound valence electrons. Plasmon peaks appear in energy-loss spectra taken from metals because their valence electrons are in the conduction band, so their orbitals are delocalized over several atomic units. That means that the sample is in equilibrium with a uniform electron density until the incident electrons pass through the specimen. This disturbance sets up oscillations in the electron density, the result of which is a loss of energy from the incident electron. Similar peaks from non-metals can be caused by the excitation of valence electrons to energy states above the Fermi level. Excitations from molecular orbitals may also give rise to peaks in this region.

While low loss peaks are not always sufficiently unique in energy to allow unambiguous elemental determination, plasmon peaks can play an important role in EELS studies. Sufficient standardization has been carried out to allow changes in plasmon peak positions and intensities to be used as a measure of changes in elemental concentrations for radiation damage studies of samples containing metals. An example of such a study is shown in figure 3.3 .

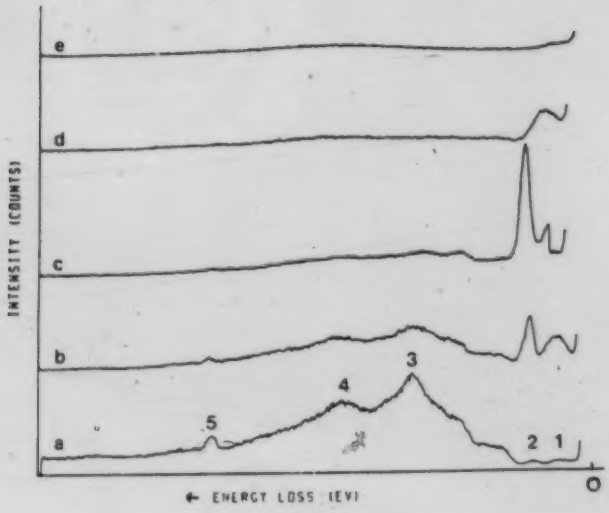

Fig 3.3) Sequence of energy loss spectra of NaCl after increments of dose have been received in the region under examination. Peaks 1 and 2 are the surface and volume plasmon losses of metalic Na, peak 3 is the plasmon peak for NaCl, and peak 5 is a core exciton doublet on the L_{2-3} edge of Na. The sequence, going from a to e, shows that irradiation turns NaCl into metallic Na, and then even removes the Na. (Muray et. al. 1984)

There are also methods for determining the thickness of the sample using the plasmon peaks. The thickness is given by taking the natural logarithm of the ratio of the total integrated intensity I_t (zero loss and low loss regions) to that of the zero-loss peak I_o and multiplying by the plasmon mean free path, λ_p (see derivation in Egerton 1986).

$$t = \lambda_p \ln(\frac{I_t}{I_o}) \qquad 3.1$$

While equation 3.1 is easy, fast and fairly accurate, the problem is that values of λ_p are not readily available. There are other methods for determining thickness such as the Kramers-Kronig sum rule calculations (Egerton and Cheng 1987), however values of t/λ_p determined from equation (3.1) can be used to indicate the importance of plural scattering effects in elemental analysis (for $t/\lambda_p \leq 1$ effects unimportant) (Egerton 1981).

3.2.3) High-Loss Region

The final region, the high-loss region, ranges from approximately 100 eV onwards, though it is rarely studied beyond a few thousand eV. The predominant characteristic of this region is the large, rapidly-falling background signal on which edges, due to inner-shell ionizations, are visible. The background is due mostly to the high energy tail of the valence electron excitations that make up the low loss

region. The angular distribution of the background is quite broad while the inner-shell's angular distribution is forward peaked, as shown in figure 3.2 .

The ionization edges are very important in EELS because they can be used to unambiguously identify each element that makes up the sample. Each edge is due to the excitation of electrons from a particular inner-shell, k,(where k = K,L,M etc.) within a particular element that is present in the sample. The threshold energy of the edge represents the binding energy of the shell and thus uniquely identfies the element involved in the interaction. With proper modeling considerations, explained in the next section, these characteristic signals lead to quantifiable information about elemental concentrations of light elements in the sample volume. It is this possibility that makes EELS so appropriate for studying mass-loss due to electron irradiation. Table 3.1 lists threshold energies for the elements with $Z \leq 28$.(A * beside the value means the edge appears in the spectra displayed in chapter 4.)

It is also possible to ascertain solid-state information about the sample from several closely related areas of study. 'Chemical shift' involves a careful study of the threshold energy of the core-loss signal, which moves (or 'shifts' by several eV) depending on the local crystallographic structure(Isaacson 1972, Johnson 1972). These shifts represent changes in the valence states at the Fermi level. Closely related is the energy-loss near-edge

TABLE 3.1

Z	Element	Edge	Position of edge (eV)
1	H	K	13.6
2	He	K	24.6
3	* Li	K	54.5
4	Be	K	111.0
5	B	K	188
6	* C	K	284
7	N	K	401
8	* O	K	532
9	* F	K	685
10	Ne	K	867
11	Na	K	1072
12	Mg	K	1305
13	Al	K	1560
		L_{23}	72
14	Si	K	1839
		L_{23}	99
15	P	K	2150
		L_{23}	136
16	S	K	2472
		L_{23}	165
17	* Cl	L_{23}	201
18	A	L_{23}	245
19	K	L_1	296
		L_3	293
		M_{23}	≃20
20	* Ca	L_1	350
		L_3	347
		M_{23}	≃25
21	Sc	L_1	406
		L_3	402
		M_{23}	~33
22	Ti	L_1	460
		L_3	454
		M_{23}	~36
23	V	L_1	520
		L_3	513
		M_{23}	~40
24	Cr	L_1	584
		L_3	575
		M_{23}	~45
25	Mn	L_1	651
		L_3	640
		M_{23}	49
26	Fe	L_1	720
		L_3	707
		M_{23}	54
27	Co	L_1	794
		L_3	779
		M_{23}	60
28	Ni	L_1	872
		L_3	855
		M_{23}	68

Shell Symbol	= Electron State	Shell Symbol	= Electron State
K	1S	L_3	$2P_{3/2}$
L_1	2S	M_{23}	3P
L_2	$2P_{1/2}$	M_{45}	3D

(A more complete list of binding energies can be found in either Colliex 1984 or Egerton 1986)

structure, ELNES, which occurs within approximately 50 eV of the threshold. Suitable theoretical calculations, in comparison to experimental results, may result in the extraction of information about local band structure(Leapman et al 1982). Extended energy-loss fine structure, EXELFS, which concentrates on the weak oscillations superimposed on the high-energy tail of the core-loss signal (50 eV to a few hundred eV from the threshold), can yield interatomic nearest-neighbour distances (Leapman 1982).

3.3)Quantification of Inner-Shell Edges

3.3.1) The Angular and Energy-Loss Distribution of Inner-Shell Scattering

The theory, which has been derived to precisely describe both the angular and energy-loss dependence of inelastic scattering, is very complicated. To give a complete derivation of the procedure is beyond the scope of this thesis. However, some understanding of the process is neccessary so that the equations used for quantification of inner-shell edges will not seem completely ad-hoc.

The basic procedure is to consider a single fast electron interacting inelastically with the electrons of an isolated atom. The interaction is considered in terms of initial and final state wave functions for each of the atomic electrons. Using the Born approximation then gives a differential cross section in terms of a differential solid angle,$d\Omega$ (Inokuti 1971). The problem can be simplified by assuming that the energy lost by the fast electron is very much less that its initial energy, and that the final state of the atomic electron is in the continuum (so that the energy-loss spectrum becomes continuous). Then the differential cross section can be differentiated for its energy-loss dependence. Thus both the angular and energy-loss dependence of inelastic scattering can be expressed by the double-differential cross section (Egerton 1986)

$$\frac{d^2\sigma}{d\Omega dE} \cong \frac{8a_o^2R^2}{Em_ov^2} \frac{1}{(\theta^2+\theta_E^2)} \frac{df(\theta,E)}{dE} \qquad 3.2$$

where: E is the energy lost by the fast electron

θ is the scattered electron's angle from the normal

$a_o=\frac{4\pi\epsilon_o\hbar^2}{m_oe^2}=.53$ Å, the Bohr radius

$R=\frac{(m_oe^4/2)}{(4\pi\epsilon_o\hbar)^2}=13.6$ ev, is the Rydberg energy

v is the velocity of the incident electron

$\theta_E=\frac{E}{(E_o+m_oc^2)(v/c^2)}$ is the 'characteristic angle'

$\hbar=\frac{h}{2\pi}$ where h is Planck's constant

The last term in 3.2, known as the Generalized Oscillator Strength (GOS) per unit energy loss, is defined by

$$\frac{df(q,E)}{dE}=\frac{E}{R} \frac{|\epsilon_n(q)|^2}{(q\,a_o)^2} \qquad 3.3$$

where $\epsilon_n=\langle\Psi_n|\sum_j \exp(i\underline{q}\cdot\underline{r}_j)|\Psi_o\rangle$

$\underline{q}$ is the scattering vector and is related to θ

$\underline{r}_j$ is the coordinate of the j^{th} atomic electron

and where $|\Psi_o\rangle$ and $|\Psi_n\rangle$ are the initial and final state wavefunctions respectively.

To evaluate the differential GOS it is necessary to know the initial and final state wave functions of the

atomic electrons, for which there are several methods of calculation. The method for calculating the cross sections used in this study employed a 'hydrogenic model' to find the wave functions. It can generate a fairly accurate K-shell (within 10%) and adequate L-shell ionization cross section very rapidly (Egerton 1979). The method involves a simple treatment of the screening of the nuclear charge by atomic electrons, thus producing a 'hydrogenic equivalent' atom with a reduced nuclear charge and no outer shells. Since this treatment allows analytic wavefunctions and thus an analytical solution of the GOS, the cross section can be calculated 'on line'.

The solution of a differential GOS, when graphed on an appropriate three dimensional axes, is known as a Bethe surface. An example of just such a solution is shown in figure 3.4 .

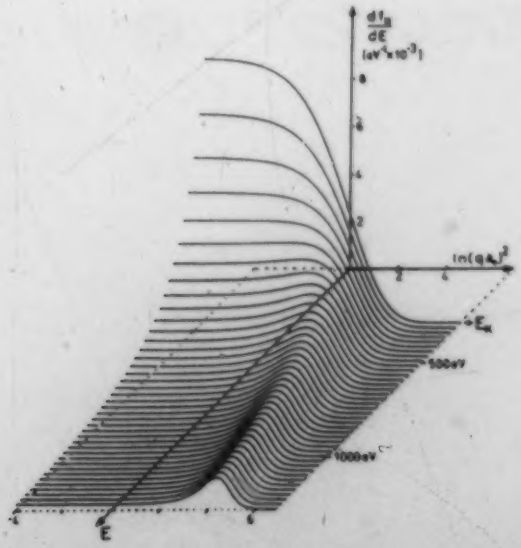

Fig 3.4) Bethe surface for K-shell ionization, calculated using a hydrogenic model (Egerton 1979). The horizontal coordinate is related to scattering angle.

3.3.2) Partially Integrated Ionization Cross Sections

The electron spectrometer has a limited collection semi-angle, β, such that electrons scattered beyond this angle are not accepted. This means that all the electrons which contribute to a particular ionization edge have been scattered by atomic electrons in a particular shell of a particular element within the sample volume, and have been scattered through an angle no greater than β. To determine the energy differential cross section for that event, equation 3.2 must be integrated over angle, up to β.

$$\frac{d\sigma}{dE} \cong \frac{4R\bar{n}^2}{(Em_o v^2)} \int_0^{\beta} \frac{df(\theta,E)}{dE} \frac{1}{(\theta^2+\theta_E^2)} \, 2\pi\theta d\theta \qquad 3.4$$

where the GOS can be calculated for each angle by the method mentioned in the previous section.

If we consider the energy-loss spectrum for a moment, we can say that the intensity due to the inner-shell ionization J_k ($J_k = J_{total} - J_{Background}$ see figure 3.6) is related to the differential cross section by the equation

$$J_k(\beta,E) \cong N \, I_t(\beta) \, \frac{d\sigma}{dE} \qquad 3.5$$

where N is the number of atoms, per unit specimen area, that contain shell k.

$I_t(\beta)$ is the total intensity transmitted through the collection semi-angle β.

By integrating the above equation over an energy window Δ, beyond the ionization threshold E_k, we obtain an equation for the integrated intensity of the edge, I_k .

$$I_k(\beta,\Delta) \cong N\, I_t(\beta)\, \sigma(\beta,\Delta) \qquad 3.6$$

where the 'partial' ionization cross section is defined by

$$\sigma(\beta,\Delta) = \int_{E_k}^{E_k+\Delta} \frac{d\sigma}{dE}\, dE \qquad 3.7$$

which can be solved quickly by numerical integration. Figure 3.5 shows solutions of equation 3.7 for some K-shells .

Equation 3.6 can be rearranged into the form in which it is used for elemental concentration calculations.

$$N \cong \frac{I_k(\beta,\Delta)}{I_L(\beta,\Delta)}\, \frac{1}{\sigma(\beta,\Delta)} \qquad 3.8$$

where I_L is the integrated intensity of the low loss region, including the zero-loss peak, up to $E=\Delta$.

The total intensity term $I_t(\beta)$ has been replaced with low loss intensity term $I_L(\beta,\Delta)$ to correct for an error which would otherwise arise because of mixed scattering in

all but the thinnest of samples (Egerton 1978). Mixed scattering is defined by an incident electron exciting both an inner-shell and one or more valence electrons as it passes through the sample. This interaction tends to move intensity beyond the integration region Δ in the ionization edge but would not remove any signal from the total intensity $I_t(\beta)$. An approximate solution to the problem is to replace the total intensity with the low loss intensity up to E=Δ. The change of terms has been shown to correct for the mixed scattering (to within 5%) as long as Δ is no less than 50 ev (Egerton, 1978).

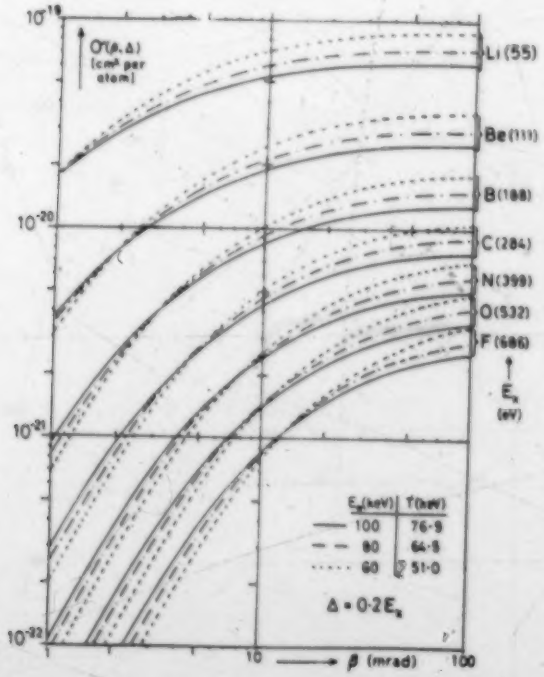

Fig 3.5) Partial cross section for K-shell ionization of second-period elements, calculated for an integration window Δ equal to one fifth of the edge energy, assuming hydrogenic wave functions and non-relativistic kinematics (Egerton 1979).

3.4) Analysis Procedure

As has been mentioned previously, the high loss region of the energy-loss spectrum consists of a steeply falling background from which the inner-shell edges protrude. In order to quantify the core loss signals, the background signal under the edge must be subtracted from the intensity. The background intensity cannot be calculated from first principles due to the complexity of its origins. The analysis procedure thus depends on the fitting of an empirical formula to the background. The formula that is applied is an inverse power law (Egerton 1986)

$$A \cdot E^{-r} \qquad 3.9$$

where E is the energy loss and A and r are the fitting parameters.

There are several methods for determining the parameters, but the simplest and fastest is probably the two-area method. Developed by Egerton (1986), the method uses a fitting region, Γ, in front of the ionization threshold, E_k. The region, which starts at E_1 and ends at E_2 just in front of E_k, is divided in half and the integrated intensity of each half is represented by I_1 and I_2 as shown in figure 3.6 . The fitting parameters can be calculated in terms of these values by using the following equations.

$$r=2\{\log (I_1/I_2)\}/\log(E_2/E_1)$$

3.10

$$A = (I_1 + I_2)(1-r)/(E_2^{1-r} - E_1^{1-r})$$

While this method is only exact for r=2, it is fast and quite accurate even for larger values of r (r is always less than 6) (Egerton 1986).

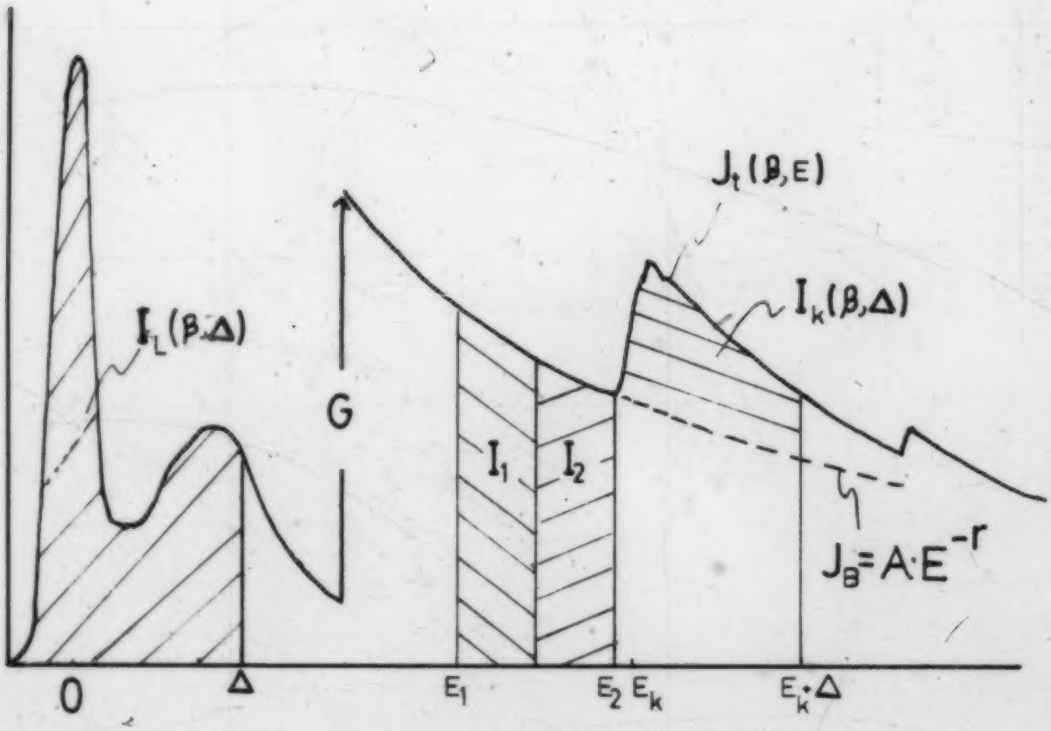

Fig 3.6) Two-area method of background fitting. Values of A and r are obtained by measuring the areas I_1 and I_2 under the background just preceding an ionizat ion edge.(Egerton 1986)

Another often used method of calculating the fitting parameters is the Least Squares method. A derivative of this method called ' weighted least squares' was employed to calculate the parameters used in this study. While the method is more time consuming for the computer, for the edges involved in this study, it did seem to give good fits more consistently than the two-area method.

Once the parameters have been calculated so that the $A \cdot E^{-r}$ curve fits the background in front of the threshold, the curve is extrapolated beyond E_k by at least Δ. (At this point the computer program allowed the experimenter to reject the edge and try a different fitting region Γ, if the extrapolation was incorrect.) The intensity of the core-loss signal, I_k, can then be calculated using the equation

$$I_k(\beta,\Delta) = \int_{E_2}^{E_k+\Delta} J_t(E)dE - \frac{A}{1-r}\left[(E_k+\Delta)^{1-r} - E_2^{1-r} \right] \qquad 3.11$$

The other value measured from the spectrum, for equation 3.8, is the low loss intensity up to Δ, $I_L(\beta,\Delta)$. This value is simply calculated by summing the intensity value (counts) from each channel in that region.

It should be mentioned that there is a small deviation from the theory due to a practical matter with the detection system. Due to the dynamic range in intensity of the scattering, there is often a 'gain' change inserted between

the low loss and high loss region. The 'gain', G, refers to a switch in the counting process from a voltage/ frequency conversion to a pulse counting (as explained in section 2.4), which appears as a jump in the spectrum(see figure 3.7). This gain was measured by fitting a curve to either side of the jump and calculating the factor that would be required to bring the lines together. This factor is taken into account by slightly altering equation 3.8 to the form

$$N \cong \frac{I_k(\beta,\Delta)}{I_L(\beta,\Delta)} \frac{1}{G \cdot \sigma(\beta,\Delta)} \qquad 3.12$$

Equation 3.12 is the equation that was used to determine the elemental concentrations within the irradiated volume of the sample. The radiation damage to the specimens was measured as the decrease in this N value as a function of dose, as will be discussed in chapter 4.

Chapter 4

Encapsulation Experiments

4.1) Introduction

The experiments discussed in this chapter were conducted to determine if encapsulating a sample reduced the sample's sensitivity to radiation damage. Both the original encapsulation experiment of Salih and Cosslett (1974) and the later study by Fryer and Holland (1983) concentrated solely on the reduction of structural damage. Therefore, of particular interest here was whether the surface coatings would reduce mass loss of the light elements and, if so, by what factor? Specimens were prepared with a carbon layer on the bottom for support. One half of each specimen was also given a top coating. This allowed comparisons between the radiation-sensitivities of the single-coated and double-coated (encapsulated) halves of the same specimen, thus removing the possibility that the comparison was affected by different thicknesses or microscope conditions.

The specimen preparation required to fabricate the partially-encapsulated specimens is described in section 4.2. Section 4.3 includes the experimental conditions and the results of an experiment on a polycrystalline, organic sample. Also included is a discussion of the results and a few conclusions which could be drawn from the data. Section 4.4 contains the equivalent material for two experiments on alkali halides.

4.2) Specimen Preparation

All the specimens were prepared as partially-encapsulated polycrystalline samples, in an evaporation system like that described in section 2.5 . The process was initiated by placing a drop of liquid soap on a microscope cover slide and then rubbing the excess off with a soft tissue. The glass slide was then placed, soap side down, approximately 14 cm above the evaporation source. Graphite rods were placed with their tips in contact, to complete an electrical circuit whose current was controlled externally.

The evaporation system was pumped down to $\sim 2 \times 10^{-7}$ torr and the liquid nitrogen trap was filled to help remove condensible gases. The rods were electrically heated in short bursts which evaporated approximately equal amounts of carbon each time. Once sufficient thickness had been deposited on the slide (as determined by the change in frequency of the quartz crystal microbalance described in section 2.5 and by equation 2.2), the system was brought up to atmosphere and the glass slide removed. The carbon film was floated off the glass in warm water and picked up on 400-mesh copper (Cu) grids.

Several of the carbon coated grids were then placed (carbon side down) in a holder attached to the microbalance. The graphite rods were replaced by a molybdenum boat. Crystals of the radiation-sensitive material to be

evaporated were placed in the boat and the system was pumped down again. The sample material was gently sublimed at a rate of ~2 A/s for approximately 50 s. The system was once again brought up to atmosphere and the specimens were removed.

The specimens were then placed in a special holder which allowed an aluminum foil to cover one half of each specimen. This holder was attached to the microbalance and the molybdenum boat was replaced by the graphite rods. Once the system was pumped down, a second carbon layer was evaporated onto the exposed portion of radiation-sensitive material. A sketch of a partially-encapsulated specimen, which results from the above preparation procedure, is displayed in figure 4.1. The left side of the diagram shows the 'single-coated half', while the right side shows the 'double-coated half'. The carbon film marked (c) is called the 'encapsulation layer'. The regions marked 'sample volume' show the actual volume that the electron beam tranverses, and thus the volume which is studied by the subsequent EELS analysis.

The absolute thickness of each layer was then determined. Following the analysis procedure for inner-shell edges described in section 3.4, the areal density N, of an element was determined for the sample volume. Assuming the sample is stoichiometric, the formula of the layer in question will give ξ, the factor to convert areal density of an element to the areal density of molecules.

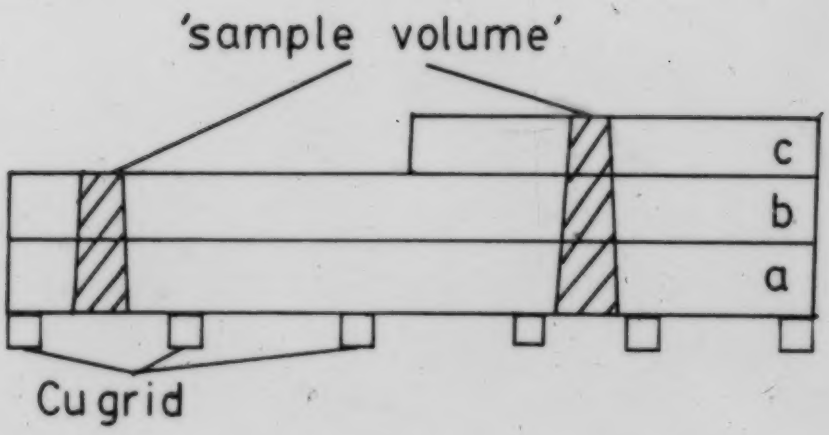

Fig 4.1) A partially-encapsulated specimen. Layers (a) and (c) are amorphous carbon films. Layer (b) is the polycrystalline, radiation-sensitive material. Dashed regions marked 'sample volume' are the volumes studied by EELS.

The first of the three radiation-sensitive materials prepared for this thesis was pentadecachlorinated copper phthalycyanine (ClCuPc) whose formula is $Cl_{15}CuC_{32}N_8H$, and whose molecular structure is displayed in figure 4.2. The other materials prepared were the alkali halides, LiF and CaF_2.

The absolute thickness of a layer (in nm) is given by the equation below.

$$t = \frac{N \xi M_m M_p}{\rho_b} \times 10^{-7} \qquad 4.1$$

where M_m is the molecular mass number

$M_p = 1.66 \times 10^{-24}$ gm, the mass of a proton,

ρ_b is the bulk density of material (g/cm^3)

Values of ξ, M_m, ρ_b, as well as the absolute thicknesses of the sample layers and their carbon coatings are listed in table 4.1. Thickness of the encapsulation layer (c) was determined by calculating the total carbon thickness and subtracting the thickness of the bottom layer (a). It should also be mentioned that the thickness calculations, for the carbon layers on the ClCuPc specimen, required a correction factor to allow for the number of carbon atoms contained in the ClCuPc molecules. The correction was made to the areal density of carbon N^C, and simply involved the subtraction of (32/15) times the areal density of Cl initially in the sample volume.

$Cl_{15}Cu\,C_{32}N_8\,H$

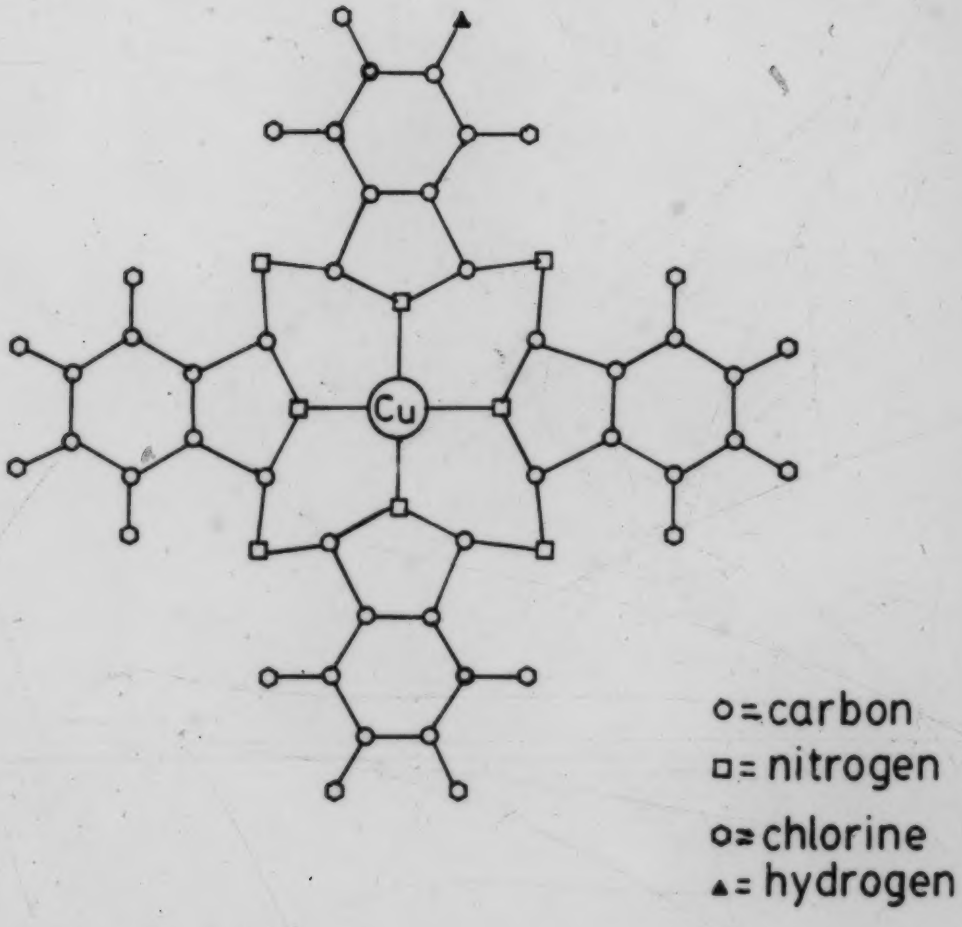

Fig 4.2) The molecular structure of pentadecachlorinated copper phthalocyanine (Uyeda et al 1972). All but one of the hydrogen atoms of copper phthalocyanine have been replaced with Cl. Note that the Cl are the most peripheral atoms in the molecule.

TABLE 4.1

Sample Material (b)	Element Analysed	ξ	M_m	ρ_b g/cm^3	Sample Thickness (nm)	Carbon Thickness (a)	(c)
ClCuPc	Cl	1/15	1093	~2	~10	10	6
LiF	F	1	25.9	2.6	13	15	9
CaF_2	F	1/2	78.1	3.2	11	12	7
Coating	Carbon	1	12	1.8			

4.3) ClCuPc

4.3.1) Experimental Procedure

For the radiation damage experiment conducted on the partially-encapsulated ClCuPc specimen, the spectrometer was image coupled to the electron microscope as described in section 2.3 (and shown in figure 2.6 b). While this configuration requires particular care to centre the diffraction pattern in the spectrometer entrance aperture, it was used to facilitate monitoring of the fading diffraction pattern (which gave information about the loss of crystal structure). Centering the diffraction pattern required that the beam tilt be altered slightly so that the centre of the diffraction pattern coincided with the centre of the smallest spectrometer entrance aperture (d=1mm). The small aperture was then switched for the largest one (d=5mm) to reduce the error in this centring process.

When the spectrometer is image coupled to the microscope, β is set by the spectrometer entrance aperture as explained in section 2.3. To determine this value it was necessary to use the diffraction pattern of a known standard, in this case Fe, to calculate the camera length (see appendix A). Also necessary for the calculation was the exact radius of the aperture. So with no specimen present, the beam was centred in the largest aperture as previously described. The beam was then expanded in small steps (by reducing the current in the condenser lenses), with the

spectrometer being refocused each time, until the beam was expanded to the diameter of the aperture, after which the zero-loss peak began to drop in height. An image of the expanded beam was recorded photographically, and the whole process repeated. The average radius of the aperture (i.e. the radius of the beam, measured from the photographs) divided by the camera length, gave β, which for this experiment was 3.8 mrad.

It was necessary to determine the irradiation 'dose rate' received by the specimen. The 'dose rate' is defined as the current per unit area received by the irradiated portion of the specimen. The incident current, I_o, was measured by focusing the beam, through a hole in the specimen, into a Faraday cup placed just above the screen. Measurement of the beam diameter was accomplished by choosing a known magnification, M (typically M=10K), and expanding the beam to a known diameter on the screen (the width of the shutter door, d_{screen}=6.3cm). The diameter of the beam, at the specimen, is then given by $d_{spec} = d_{screen}/M$. The dose rate is given by the beam current divided by the irradiated area i.e.

$$\text{dose rate} = I_o/\{\pi\ (\frac{d_{spec}}{2})^2\} \qquad 4.2\ .$$

The experiment consisted of completing several computer automated 'runs' on either side of the sample. A 'run' consists of acquiring between 5 and 7 spectra, over a period

of approximately 30 minutes, from the same irradiated sample volume. Each spectrum was acquired in 50s as a single forward scan with a dwell time of 50ms per channel and an energy increment of 1 eV per channel for 1024 channels. A couple of runs were made on both the double-coated (encapsulated) portion and the single-coated side of the specimen, before the process was repeated.

In moving from the thicker double-coated side to the thinner single-coated side, the intensity of the beam entering the detector became too great and the zero-loss peak saturated at the 1.2 MHz mentioned in section 2.4. Since it was not possible to change either I_o (it would change the dose rate) or the spectrometer entrance aperture (which would change β), it was necessary to vary the field limiting (selected area) aperture described in section 2.2.

The diffraction pattern was monitored between successive spectral aquisitions; it was recorded at the start of the irradiation run, and after such time that the bright diffraction ring had become indistinguishable from the diffuse background.

After each spectrum acquisition, the computer program automatically subtracted the instrumental background from the low-loss region and calculated the value of the gain G as explained in section 3.4. The irradiation time T_k, the time from the start of the irradiation run to the time the particular edge was acquired, was also recorded. The signal being monitored in this experiment was the chlorine (Cl)

L-edge, which has its threshold at E_k=200 eV. The quantification of the inner-shell signal I_k followed the procedure outlined in chapter 3, with the background fitting region Γ=70 eV and the integration window Δ =50 eV. The program calculated the signal ratio $\frac{I_k}{I_L}$, which with the partial ionization cross section $\sigma(\beta$=3.8mrad,Δ =50eV) = 2.53×10^{-20} cm^2, was used to calculate N^{Cl} (as expressed in equation 3.12). The accumulated dose D was determined by multiplying the dose rate by T_k. The mass loss of the Cl atoms from the ClCuPc sample could then be displayed, in its quantified form, by graphing N^{CL} vs D .

4.3.2) Results and Discussion

As mentioned in chapter 1, the fading of the electron diffraction pattern is an indication of the structural damage occurring in the sample. To determine if the encapsulation had any effect on the rate at which structural damage occurred, it was necessary to define a stage in the fading, which occurred for both the single coated and double coated sample, that could be used as a basis for the quantification. A characteristic dose D_f was defined as the dose required for the brightest diffraction ring to become indistinguishable from the diffuse background.

Figure 4.3 shows typical diffraction patterns for the single-coated side of the specimen, at the start of the irradiation run and after exposure to the characteristic

Fig 4.3) Typical diffraction pattern for polycrystalline ClCuPc (a) at start of irradiation run and (b) after $4.2C/cm^2$.

dose. The average characteristic doses for the single-coated and double-coated halves of the sample were 3.8±.6 C/cm^2 and 5.2±.4 C/cm^2 respectively. It is possible to define a protection factor as the ratio of characteristic dose obtained for the encapsulated half to that of the single-coated half. Thus the structural protection factor for ClCuPc was 1.4±.3, which is substantially lower than the values of 6 to 9 determined for epitaxial samples studied by Fryer and Holland (1983).

Figure 4.4 shows typical energy-loss spectra recorded from the single-coated side of the ClCuPc sample, (a) at the start of the irradiation and (b) after an accumulated dose of 4.2 C/cm^2. The loss of Cl from the sample volume is apparent from the decreased intensity of the inner-shell signal.

The Cl concentration (per unit area) N^{Cl} is plotted as a function of accumulated dose D in figure 4.5 . This display of the mass loss represents an average of 4 irradiation runs from the single-coated side and 3 runs from the encapsulated side. For mass loss, the characteristic dose $D_{1/2}$ can be defined as the dose required to reduce the concentration of an element to 1/2 of its original value. For the single-coated sample $D_{1/2}$=2.6 C/cm^2, while for the double-coated side $D_{1/2}$ =6.0 C/cm^2, which gives a protection factor of 2.3 for the mass loss of Cl from polycrystalline ClCuPc.

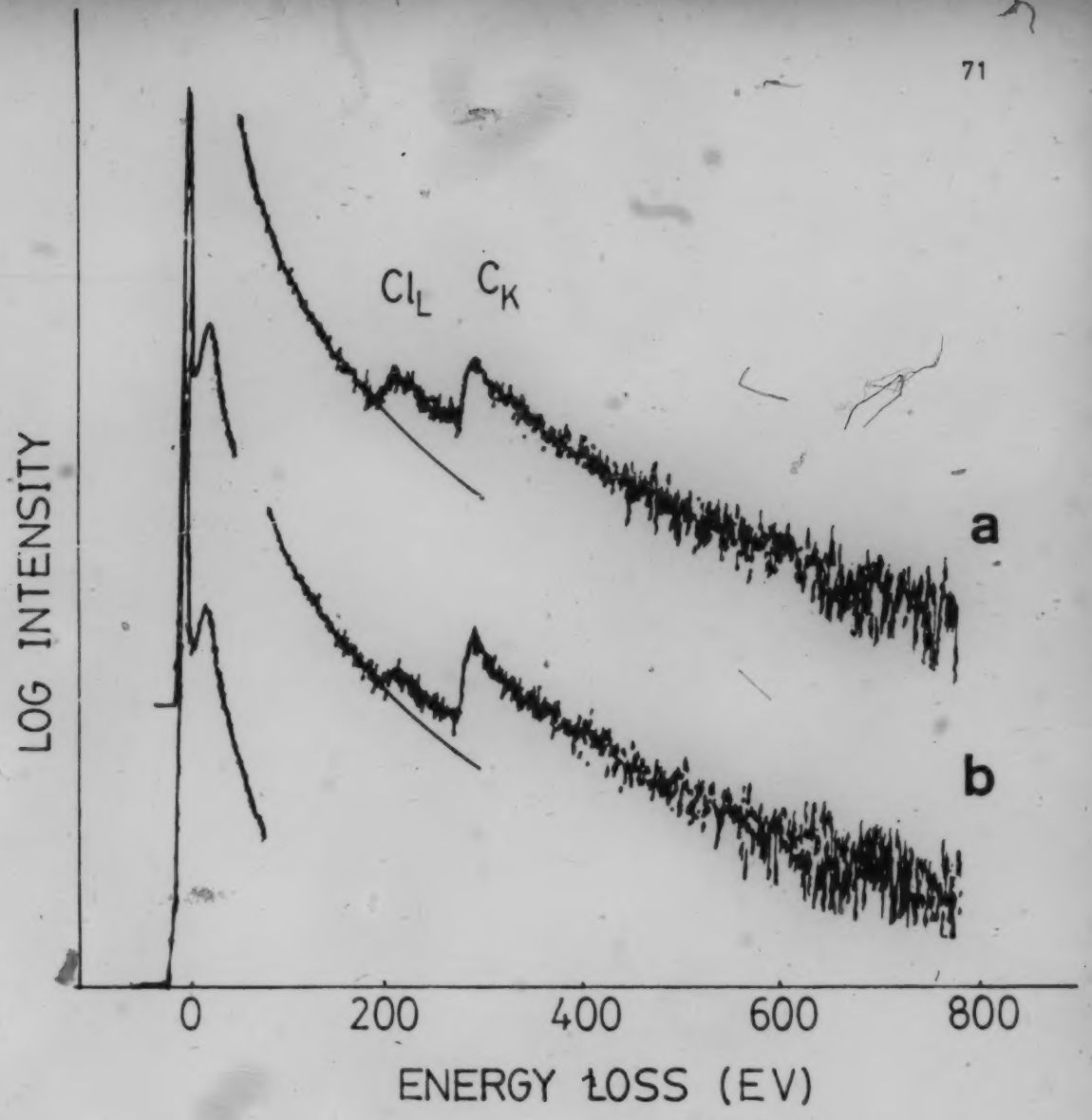

Fig 4.4) Typical electron energy-loss spectra of ClCuPc (a) at start of irradiation run and (b) after 4.2C/cm^2. Spectrum (a) has been shifted vertically to allow clear visibility of all edges. Chlorine L-edge is shown with fitted background. Spectrometer was image coupled with collection semi-angle β=3.8mrad and dose rate of 4.8x10^{-3}A/cm^2.

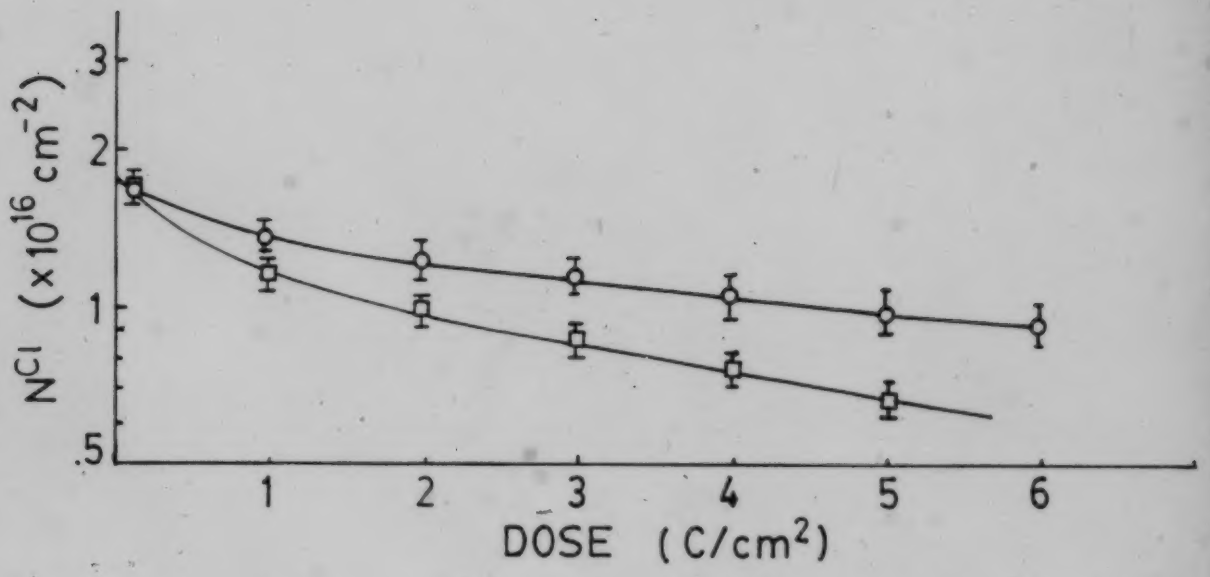

Fig 4.5) Areal density N^{Cl} of chlorine in ClCuPc as function of exposure to 80keV electrons. Bottom line is for single-coated sample and has $D_{1/2}$=2.6 C/cm^2. Top line is for double-coated sample and has $D_{1/2}$=6.0 C/cm^2. (Error bars in all graphs represent one standard deviation in the averaged values.)

The first observation that can be made is that the encapsulation reduced the mass loss more effectively than it did the structural damage. This is perhaps not surprising since structural damage can occur without mass loss, whilst the reverse is not true. So it is possible for the encapsulation to completely stop mass loss without reducing the structural damage at all, but not the reverse.

The damage mechanism, as explained in chapter 1, is one of bond scission, but it must also include bond fusion (Fryer 1984). The peripheral halogen atoms (Cl) are preferentially 'freed' from the molecule by bond scission. With the parent molecule still in its proper lattice position, the free halogen atoms may recombine and thus no permanent structural damage will occur. If, instead, the free halogen atoms diffuse away from the parent molecule, the molecule may degrade into molecular fragments (irradiation-induced degradation), or fuse with other nearby damaged molecules (cross-linking), thus permanently altering the crystal structure (Fryer 1984).

Clark et al(1980) invoked the 'cage effect' to explain why the ClCuPc crystals damaged preferentially at exposed surfaces and at interior defect sites. Within a perfect crystal, any molecular fragment or atom scissioned from the molecule is forced to remain in close proximity, because no diffusion routes are accessible, thus making recombination more probable. The cage effect is weakest around the edges of the crystal, and thus damage occurs most rapidly there

(Smith et al 1986). The cage effect is also quite weak at the crystal defect sites and at planes adjacent to already damaged molecular planes ('damage front'), thus damage proceeds at an intermediate rate there (Smith et al 1986). It has also been shown that for ClCuPc crystals, which are less than fully chlorinated (ie. less than 16 Cl per molecule), there is an increase in the number of internal damage sites as the exposure accumulates (Clark et al 1980). This may be due to an overall weakening of the cage effect because there is more room (around the the remaining hydrogen atoms) for the Cl atoms to diffuse away from their parent molecules.

The polycrystalline $Cl_{15}CuPc$ sample studied here, unlike the single crystals, possesses a large number of internal grain boundaries, as shown by figure 4.6. The free Cl may diffuse from the small crystallites into the grain boundaries, which due to their preferential damage rate, offer a quick route to the surface with little chance of recombination.

If it is assumed that all the Cl freed from the parent molecules managed to immediately escape, it is possible to derive an argument for the mechanism by which the encapsulation extends the lifetime of the crystal structure. After an accumulated dose D_f= 3.8 C/cm^2, figure 4.5 shows the percentage of Cl 'freed' to be approximately 60% of the initial value. It is possible that this value is comparable to that required to completely damage a single

a)

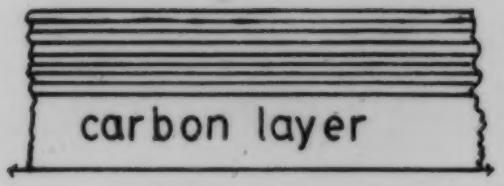

b)

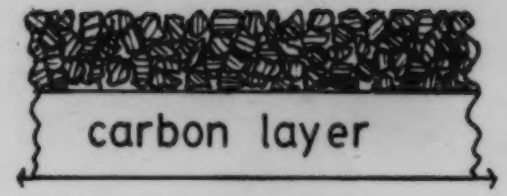

Fig 4.6) Examples of (a) single crystal and (b) polycrystalline structure. The lines in the crystals represent lattice planes. Note that there are many grain boundaries as well as gaps between crystallites in (b).

crystal. According to Clark et al (1980), an X-ray microanalysis of a single crystal, which had received a dose sufficient to completely fade the diffraction pattern, showed only a ~15% loss of Cl. It seems likely then, that a large number of Cl (~45%) were freed from their parent molecule, but did not escape from the crystal. This would tend to suggest that in a large single crystal, Cl atoms are not able to diffuse very far. Further evidence of this short diffusion length comes from HREM micrographs from a study of damage to single crystals of ClCuPc (Smith et al 1986). They show that molecules within only 3 or 4 lattice sites of a damaged plane ('damage front') are unaffected. It would seem that the Cl gain barely sufficient energy from the scission process to move past the nearest couple of partially damaged molecules, and are thus unlikely to diffuse very far in the damaged (cross-linked) region. The evidence thus suggests that, for a large single crystal, the lost Cl atoms more than likely come from the surface layers only.

Fryer (1984), having conducted an encapsulation study on epitaxially prepared, single crystal $Cl_{16}CuPc$ concluded (from diffraction information) first that the encapsulation layer stopped the Cl from leaving the crystal, and secondly that this increased the Cl partial pressure within the crystal and resulted in an enhanced recombination rate throughout the crystal. From the information presented so far it would seem that neither conclusion is quite correct. Figure 4.5 does prove that a carbon encapsulation layer

reduces the rate at which Cl escapes from the sample volume, though it does not seem to stop the loss. In addition, the previous argument suggests that this reduction in mass loss does not increase the recombination rate in the bulk, but only at the surface from which the Cl were lost. Since the surface is the major damage site for the crystal, the increased efficiency (due to coating) of the cage effect there would increase the radiation resistance of the entire crystal. It would do so by increasing the time it takes for the initial 'damage front' to form at the surface, where it must form before it can work its way into the bulk. Thus the recombination rate in the bulk is never increased; it simply remains constant for a longer period of time.

This conclusion is further supported by the small structural protection factor for the polycrystalline sample. Only the small fraction of the grain boundaries adjacent to the carbon layer are affected by encapsulation. Thus no great improvement in the radiation resistance of the sample could be expected.

It is not clear precisely what mechanism is responsible for reducing mass loss. It has been suggested that the carbon layer may absorb free Cl atoms, but retain them within the irradiated volume (Egerton at al 1987). Since this action would not explain the slower loss of crystallinity, it is not likely to be the only mechanism in this case. It is also possible that the carbon layer simply worked as a diffusion barrier. The path which the Cl follow

to leave the sample volume would be lengthened by collisions with the carbon atoms. This diffusion barrier effect would also increase the lifetime of the crystal structure, as explained earlier.

4.3.3) Conclusion

There are a few conclusions which can be drawn from the radiation damage experiment on partially-encapsulated, polycrystalline $Cl_{15}CuPc$. First, the encapsulation did reduce the mass loss of Cl by a factor of 2.3. Secondly, the encapsulation slightly increased the lifetime of the crystal structure by a factor of 1.4 . While both protection values are less than ideal, the information gained from the experiment does offer some encouragement. From the information presented here and in the literature (as referenced in section 4.3.2), it is possible to conclude that for organic crystals which damage preferentially at the surface, encapsulation is likely to be more efficient at protecting large single-crystal samples than polycrystalline ones. This is because encapsulation seems to result in an increase in efficiency of the cage effect at the layer adjacent to the carbon film.

4.4)Alkali Halides

4.4.1) Experimental Procedure

For the radiation damage experiments conducted on the partially-encapsulated LiF and CaF_2 specimens, the spectrometer was diffraction coupled to the electron microscope as described in section 2.3 (and figure 2.6 a). This mode of operation was adopted because a preliminary investigation showed that the diffraction information was ambiguous due to the occurrence of oxidation during irradiation. When the spectrometer is diffraction coupled, β is determined by the objective aperture. The value of β was established by previous microscope users to be β = 12.2 mrad. The dose rates for the experiments were determined as described in the previous section (see equation 4.3). Dose rates of 5.7×10^{-3} A/cm^2 for LiF, and 6.4×10^{-2} A/cm^2 for CaF_2 were used to obtain significant mass loss within an acceptable time limit.

The experiments consisted of completing several automated runs on both halves of the specimen. Each spectrum was acquired in 50s as a single forward scan with a dwell time of 50ms per channel and an energy increment of 1 eV per channel for 1024 channels.

Once again, in moving from the double-coated to single-coated portion of the specimen, the intensity of the beam entering the detector became too great. Varying the spectrometer entrance aperture was found to give too coarse

a change in intensity. To maximize the signal without saturating the zero-loss peak, varying the magnification of the image was found to give a much finer control of the intensity entering the detector.

According to Hobbs (1984), the element most likely to suffer knock-on damage in these samples is lithium (Li), due to its small atomic mass. Due to the reduction in the energy required to displace an atom at the surface (as compared to the bulk) and the directionality of the momentum transfer, as explained in chapter 1, knock-on damage at the exit (bottom) surface results in sputtering of the atoms (Hobbs 1984,Thomas 1985). The loss of Li at the exit surface should create free F atoms which are then able to leave the sample relatively easily. A carbon layer covering the exit surface would presumably retard the sputtering rate and the subsequent loss of F, while a carbon layer on the opposite surface (top) would not. To determine if knock-on damage was one of the mechanisms involved in the radiation damage, runs on both the double-coated and single-(bottom)-coated sides of the LiF specimen were completed and then the specimen was turned over; with the single coating on top, several more runs were carried out.

As in the previous experiment, after each spectrum was acquired, both G and irradiation time T_k for each edge were calculated. The signals monitored in these experiments were the oxygen K-edge at E_k=532 eV and the fluorine (F) K-edge at E_k=685 eV. Occasionally the carbon K-edge was measured to

determine if a carbon contamination layer was building up on the specimen. All edges were analysed as outlined in chapter 3, with Γ=70 eV and Δ=50 eV. The cross sections, determined by a 'hydrogenic model', were $\sigma^O = 1.1 \times 10^{-21}$ cm^2 for oxygen, and $\sigma^F = 5.63 \times 10^{-22}$ cm^2 for F (and $\sigma^C = 5.48 \times 10^{-21}$ cm^2 for carbon)

Occasionally images of the damaged region were recorded along with their diffraction paterns.

4.4.2) Results and Discussions

Figures 4.7 and 4.8 show typical energy-loss spectra recorded from single-coated LiF and CaF_2 (a) at the start of the irradiation run and (b) after significant mass loss. All spectra display their fitted background curves for the F K-edge, to help indicate the loss in intensity of the inner-shell signal. Both figures show a loss of F and a gain in oxygen with increasing dose.

Figure 4.9 shows the number of F atoms per unit area as a function of dose D, for (a) the single-coated LiF and (b) the double-coated LiF. All points represent the average of at least 4 irradiation runs. The dashed line (c) represents the number of oxygen atoms per unit area in the single-coated sample.

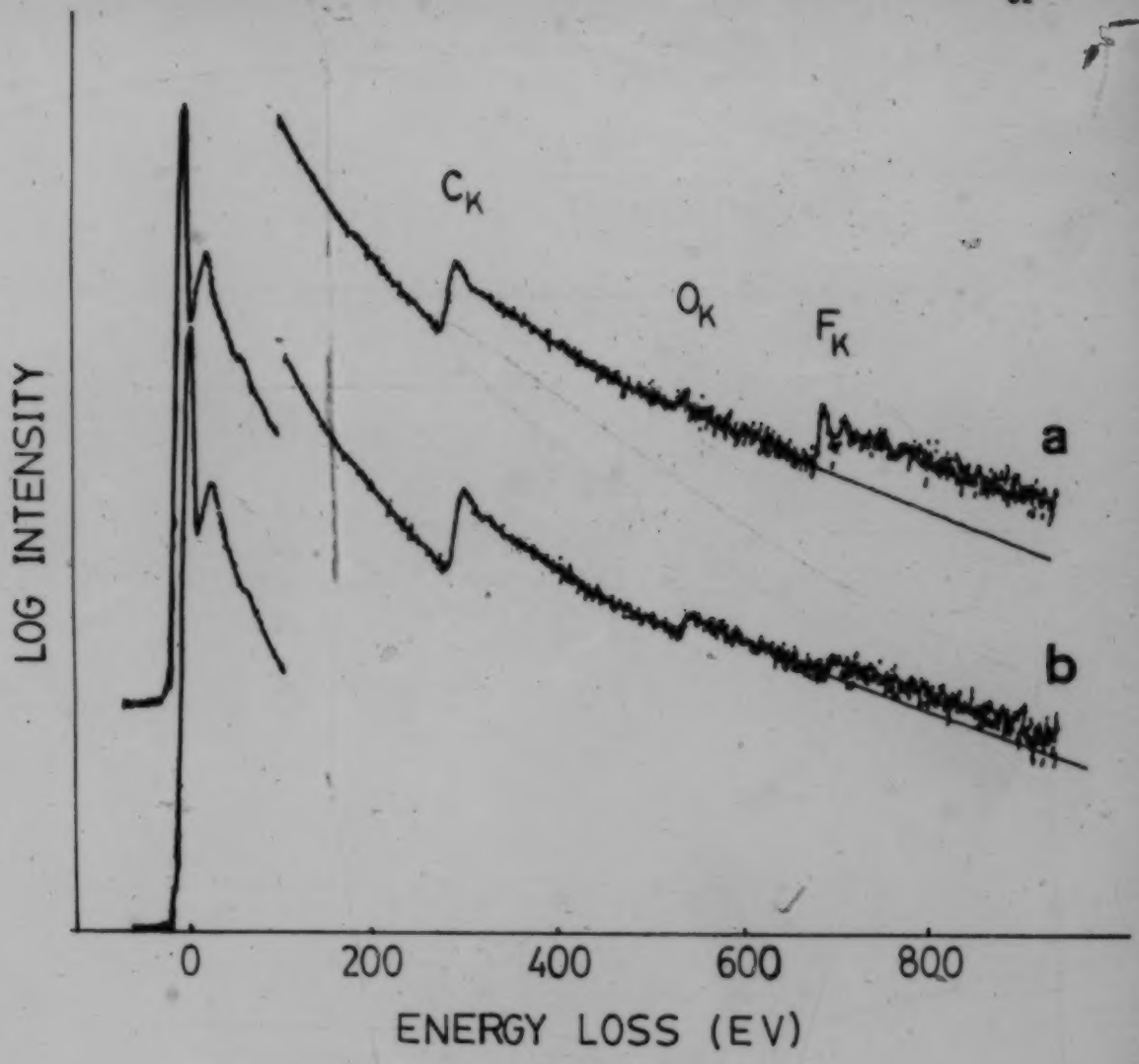

Fig 4.7) Typical energy-loss spectra of LiF (a) at start of irradiation run and (b) after 8.7 C/cm^2. Spectrum (a) has been shifted vertically to allow clear visibility of all edges. Spectrometer was diffraction coupled with β=12.2mrad and dose rate=5.7×10^{-3} A/cm^2. Flourine K-edge is shown with fitted background for clarity. Note gain in oxygen edge.

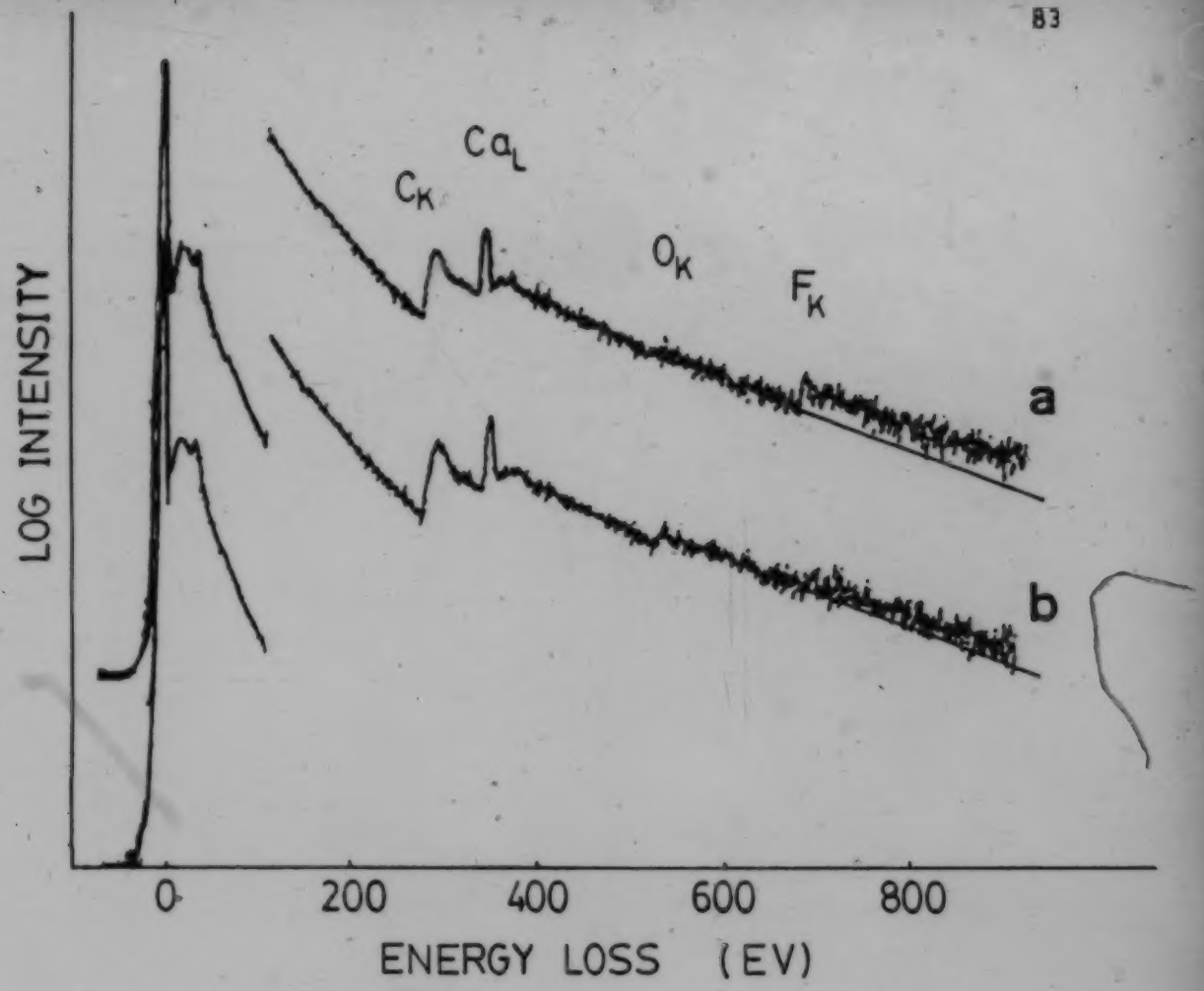

Fig 4.8) Typical energy-loss spectra of CaF_2 (a) at start of irradiation run and (b) after 200C/cm^2. Spectrometer was diffraction coupled with β=12.2mrad and dose rate 6.4×10^{-2}A/cm^2. Fluorine K-edge is shown with fitted background. Note gain in oxgyen edge.

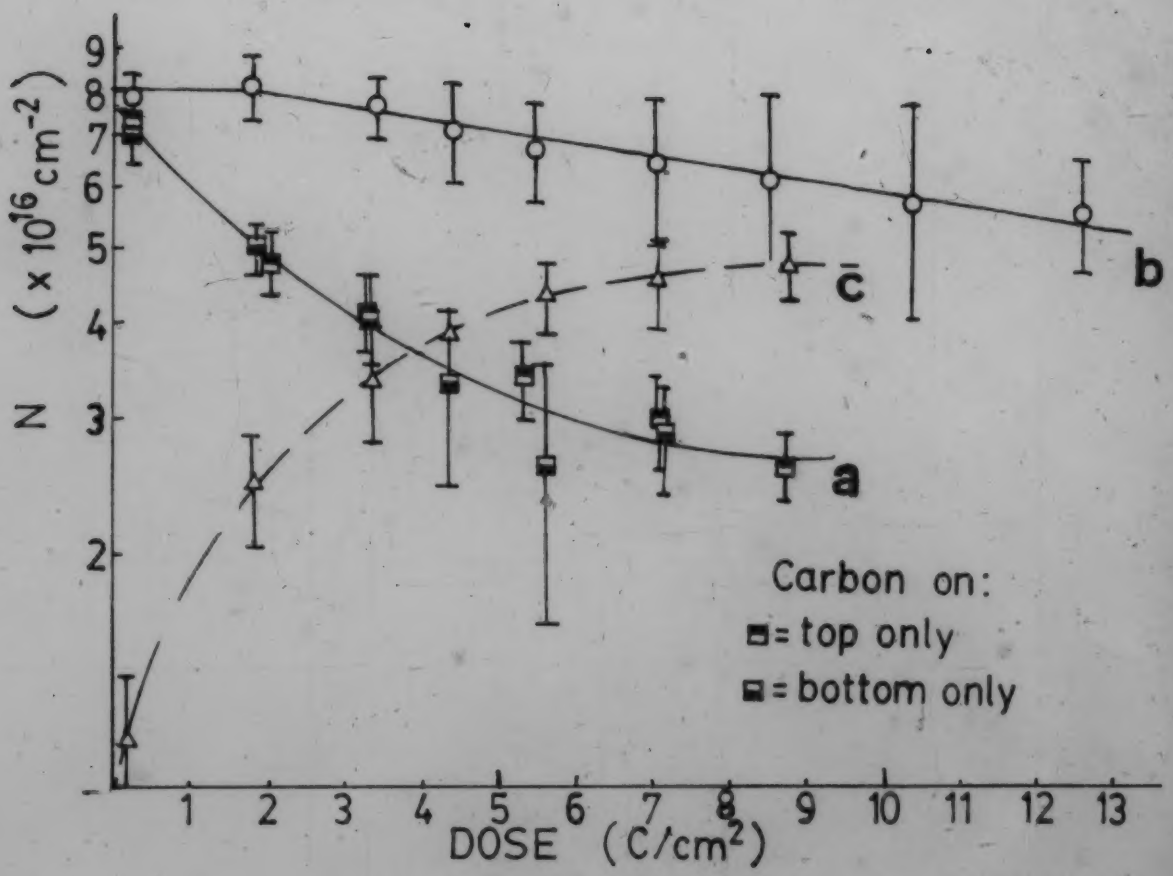

Fig 4.9) Measured areal densities N in LiF, as function of exposure to 80keV electrons. (a) is the fluorine density in the single-coated sample for which the characteristic dose $D_{1/2}$ was 3.4 C/cm^2. (b) is the fluorine density in the double-coated sample for which $D_{1/2}$=21.5 C/cm^2. (c) is the oxygen density in the single-coated sample.

It should be noted that not only did the encapsulation layer greatly reduce the rate of F loss, but there is an apparent delay in the onset of the loss ('latent dose '). Using the same definition of characteristic dose as in the last section, for the single-coated side $D_{1/2}$= 3.4 C/cm^2 and for the double-coated side (by extrapolation of line b) $D_{1/2}$= 21.5 C/cm^2. Thus the encapsulation yields a protection factor of ~6.3 for reducing F loss from LiF.

Line (a) contains points measured from the single-coated LiF when the carbon was on the bottom surface only, as well as the top surface only. The lack of any difference in the kinetics, as discussed in experimental procedure (section 4.4.1), is evidence that knock-on damage was not the predominant mass loss mechanism for the alkali halides.

Considering the gain in oxygen, line (c) shows that the number of oxygen atoms per unit area has increased by approximately 4×10^{16} cm^{-2}, which is half of the total areal density of lithium atoms in the sample volume. This shows that the LiF is almost completely oxidized to Li_2O due to irradiation induced oxygen absoption.

Figure 4.10 shows the number of F atoms per unit area as a function of dose for (a) the single-coated CaF_2 and (b) the double-coated CaF_2. All points represent the average of at least 4 irradiation runs. The dashed line (c) represents the number of oxygen atoms per unit area in the single-coated sample.

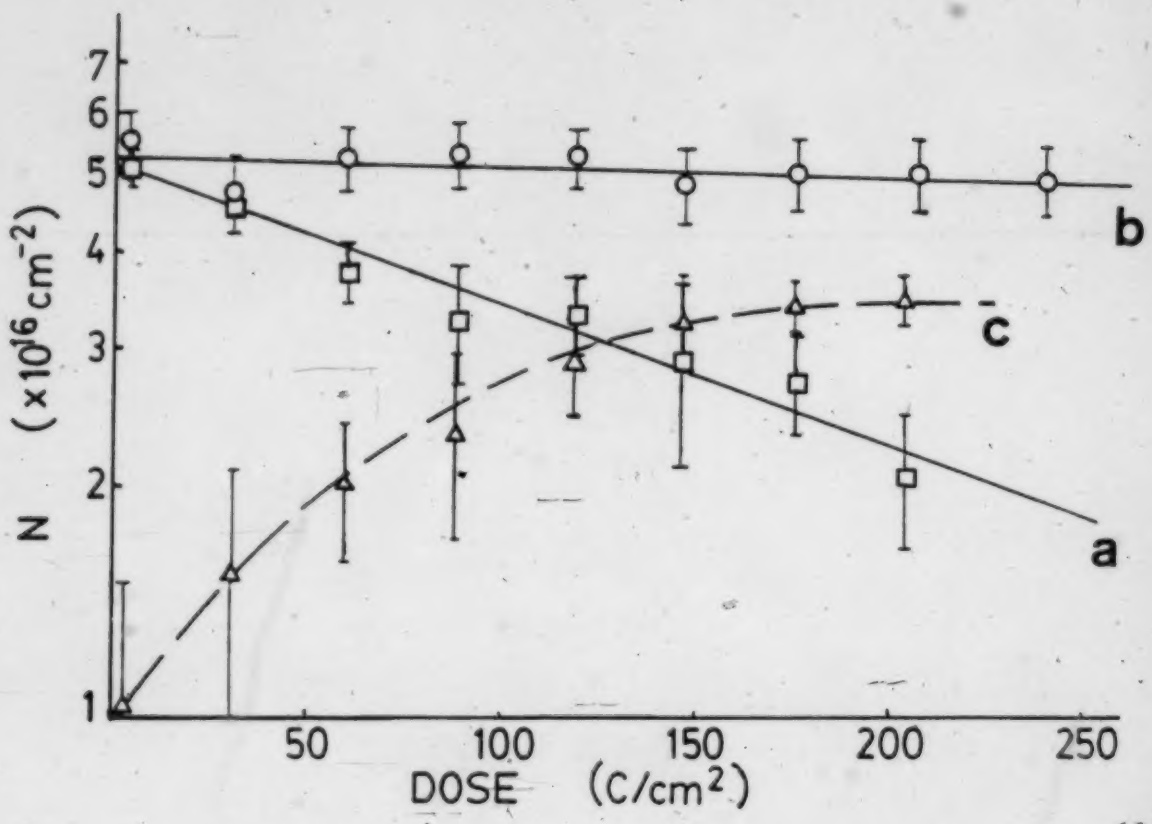

Fig 4.10) Measured areal density N in CaF_2, as function of exposure to 80keV electrons. (a) is the fluorine density in the single-coated sample and has characteristic dose $D_{1/2}$ of 168 C/cm^2 . (b) is the fluorine density in the double-coated sample and has $D_{1/2} \simeq 1700$ C/cm^2. (c) is the oxygen density in the single-coated sample.

Once again the encapsulation greatly reduced the rate at which the F was lost from the sample volume. The characteristic dose for the single-coated side was $D_{1/2}$= 168 C/cm^2, while (by extrapolation of line b) for the double-coated side $D_{1/2} \simeq$ 1700 C/cm^2. Thus the encapsulation gave a protection factor of ~10 for the reduction in mass loss of F from CaF_2.

Considering the gain in oxygen displayed by line (c) in figure 4.10, the increase in the number of oxygen is approximately 2.5×10^{16} cm^{-2}, which is equal to the areal density of calcium in the same volume (number of calcium is half of the initial F). Thus the sample is approaching complete oxidation as CaO due to the irradiation.

Further evidence of the extensive oxidation of damaged regions in both of the specimens is given by their diffraction pattern as displayed in figure 4.11. Micrographs (a) and (c) are diffraction patterns from undamaged, single-coated LiF and CaF_2 respectively. Micrographs (b) and (d) are diffraction patterns from the damaged regions of LiF and CaF_2 respectively. Figure 4.11 shows the effects of permanent alterations in crystal structure by the fading of the rings belonging to undamaged sample and the creation of rings belonging to Li_2O and CaO crystal structures.

Due to the nature of the encapsulation experiments, it was necessary to take all possible precautions to ensure that carbon contamination of the single-coated sample volume

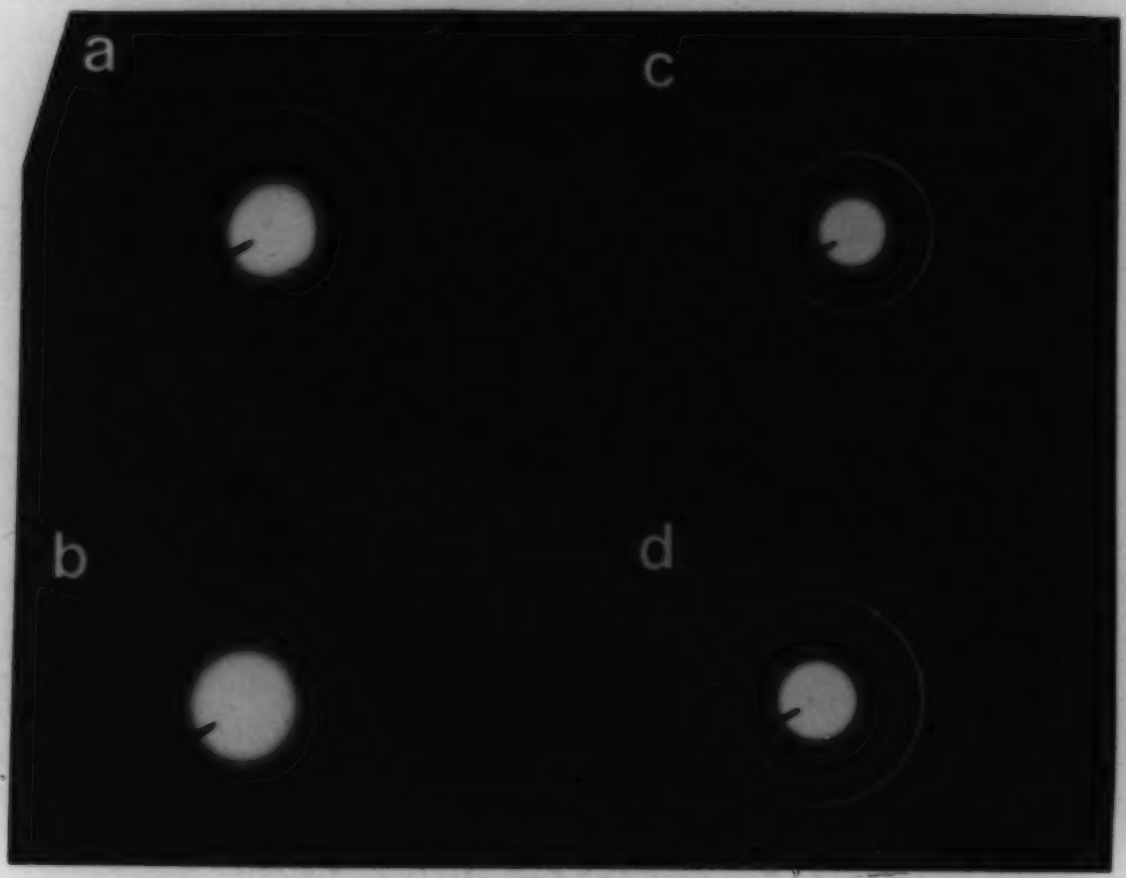

Fig 4.11) Typical diffraction patterns observed during the experiments.

INDICES (hkl)

Ring # (from center)	(a) LiF	(b) LiF	(b) Li_2O	(c) CaF_2	(d) CaF_2	(d) CaO
1	111		111	111	111	
2	200	111	200	200	200	111
3	220	200		220		200
4	311		220	311	220	
5	222	220	311	222	311	220

did not adversely affect the outcome. To this end, an anti-contamination device was employed to reduce the rate of carbon build up. Another precaution was to irradiate a larger area than was sampled. An example of how this helped is shown in figure 4.12. The area to the left, marked A, is undamaged specimen and the crystallites appear as small dark spots. The area to the right, marked B, is damaged specimen and shows an abscence of spots. The region between the dashed lines, marked C, shows that the carbon contamination, due to the polymerization of hydrocarbons by the electron beam, was concentrated at the perimeter of the irradiated region. Since the sampled area's diameter was only the centremost 1/3 of the diameter of the irradiated region (B+C), the carbon contamination should not have effected the experiments. Proof that these precautions worked is given by figure 4.13, which shows the areal density of carbon as a function of dose for (a) the single-coated LiF and (b) the double-coated LiF. The fact that neither line shows any increase is evidence that carbon contamination did not effect the experiments.

As explained in chapter one, the major damage mechanism in the alkali halides is radiolysis. While radiolysis explains the creation of Frenkel point defects in the crystal, it does not directly account for the mass loss of halogen atoms from the crystal surface (Hobbs 1984). The mass loss mechanisms for single crystals may include

Fig 4.12) Transmission electron micrograph displaying an undamaged region marked (A), in which the crystallites appear as small black dots. A damaged region marked (B), which shows very few crystallites. A region of carbon contamination with some kind of structural build up is marked (C).

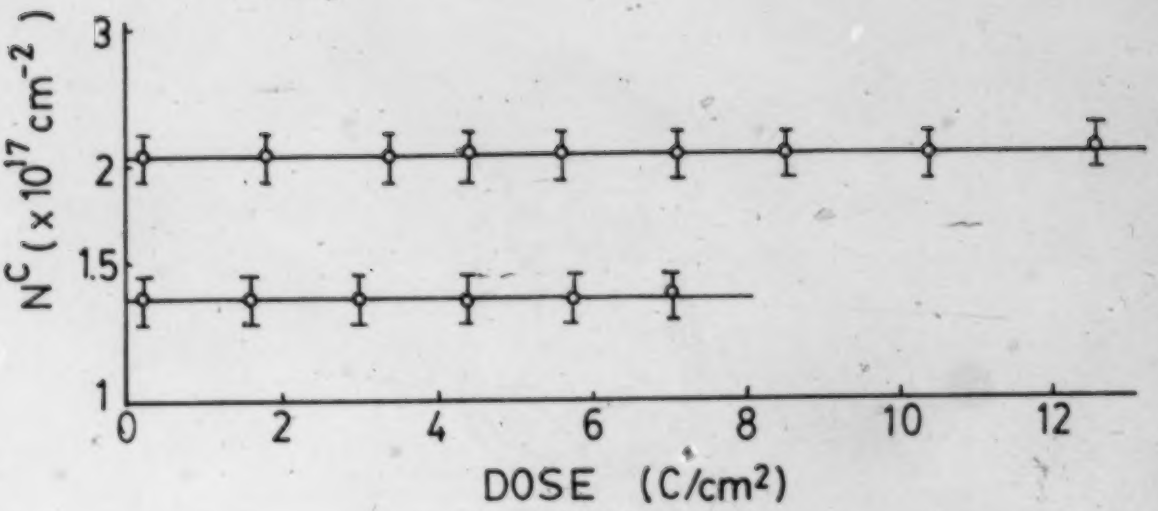

Fig 4.13) Measured areal density of carbon N^C, in the LiF sample, as a function of dose. The bottom line represents the single-coated side and the top line represents the double-coated side. All points represent the average of at least 4 runs. The lines show no increase in carbon during the experiment.

the migration of the exciton state to the surface before de-excitation (Townsend and Lama 1983), a focused replacement collision sequence after production of a Frenkel pair near the surface (Szymonski and de Vries 1983), and the possibility of knock-on damage (Hobbs 1984). The polycrystalline nature of the samples slightly modifies the possibilities for mass loss. While all the mechanisms can still function at the specimen surface (Szymonski and de Vries 1983), they can also function at internal crystal surfaces where gaps between crystallites occur, thus releasing F into the grain boundaries where it can diffuse to the surface and escape.

It has been found in ultra-high vacuum experiments that the loss of halogen from the surface can result in the residual material forming a containment layer which retards (and can even stop) the sputtering rate (Szymonski and de Vries 1983). For the two experiments described in this section, the irradiated portion of the single-coated half of the specimen became oxidized. It is not known to what extent this slowed the rate of direct sputtering, but it clearly did not stop the loss of F. The Li_2O and CaO crystals which gave rise to the diffraction rings displayed in figure 4.11 must be quite small as they are not visible in the micrographs of the oxidized regions as shown by figure 4.12. It is possible that these small crystals left gaps at the surface through which the free F could escape.

The encapsulation layer must then have effected the mass loss in a couple of ways. First, since the energy available for the sputtering process is not sufficient to sputter through thin contamination layers (Townsend and Lama 1983), the encapsulation layer could certainly have stopped all direct sputtering from the surface. Secondly, it could have reduced out-diffusion from the specimen in one of two ways. It could have acted as a diffusion barrier, slowing the departure of F by lengthening its escape path (as described in section 4.3.2). Or it could have acted as an 'absorbing layer', bonding the F to the carbon for some time, thus keeping the F within the irradiated sample volume. This latter mechanism might explain the 'latent dose' effect shown by LiF in figure 4.9 (line b).

Also worth discussing is the apparently superior resistance to irradiation damage displayed by CaF_2. The ratio of the characteristic doses for their single-coated sides was close to 50. There are two factors that might help explain this phenomenon.

One of the possible explanations is that the CaF_2 specimen contained larger crystallites than the LiF. This could have a number of effects on the rate of mass loss. Larger grains mean fewer grain boundaries for the free F to diffuse through. In addition, since the defects created in the interior of the crystallites have further to travel within the crystal before they can escape, they are more likely to recombine to form a proper lattice. It is also

possible that this longer path allows the F to aggregate and form dislocation loops or even gas pockets (Hobbs 1984), thus holding the F within the sample volume.

Another possible explanation lies within the damage process itself. According to Kabler and Williams (1978), there is evidence to suggest that the radiolysis process includes a rotation translation of a halide ion pair (bound by a self trapped hole) into an F-H configuration (Frenkel defects with small separation) with specific orientations within the lattice. For LiF these reoriented states are short lived and result in separated F-H defect pairs. But for CaF_2, one of the reorientations is metastable and results in radiative electron-hole recombination (radiative exciton decay) which restores the perfect lattice. If this is true, then CaF_2 would seem to have a fairly efficient method for releasing its energy radiatively rather than kinematically, thus significantly reducing its radiation sensitivity.

4.4.3) Conclusion

There are a few conclusions which can be drawn from the radiation damage experiments on partially-encapsulated, polycrystalline LiF and CaF_2 specimens. First and foremost is that encapsulation greatly reduced the rate of mass loss of F from the alkali halides. Protection factors of 6 and 10 respectively are large enough to significantly improve the

prospects for high-spatial-resolution microscopy and microanalysis.

The encapsulated LiF showed a delay in the onset of mass loss (latent dose), though it is not known to what extent the crystal structure was compromised during that time period. Nevertheless, the phenomenon is encouraging since it means the sample retained its stoichiometric composition even after a dose several times that necessary to acquire an energy-loss spectrum or to take several pictures. It is quite possible that other samples may show the same latent dose effect.

It is also possible to conclude that the CaF_2 specimen was much less sensitive to radiation damage than the LiF specimen, though the exact cause of this difference is not known. It is also worth noting that the encapsulated CaF_2 showed almost no loss of F over the entire extent of the experiment.

Chapter 5

Concluding Statements and Suggestions For Further Study

The experiments were successful in accomplishing the goals which they were designed to achieve. They provided quantitative evidence of the effect of encapsulation on the rate of mass loss. The experiment discussed in section 4.3 showed that the encapsulation reduced the mass loss of Cl, from ClCuPc, by a factor of 2.3. The experiments discussed in section 4.4 showed that the encapsulation reduced the mass loss of F, from LiF and CaF_2, by factors of 6.3 and 10 respectively.

The protection factors given above indicate that encapsulation was several times more effective on the alkali halides than the organic sample. One of many possibilities for further study would be to determine how much of this phenomenon is due to the difference in the damage mechanism, and how much is due to the fact that the element (whose escape is being monitored) is different. A suitable specimen material for such a study would be sodium chloride (NaCl). It is an alkali halide, so it damages like the LiF and CaF_2, but the element which suffers the mass loss is Cl, as in the organic sample. Such a study could lead to a greater understanding of the mechanism by which encapsulation reduces mass loss.

If the argument for a structural protection mechanism, expressed in section 4.3, is correct, one of the

implications would be that encapsulation should prove more effective at reducing the structural damage to single crystal ClCuPc samples, as opposed to the polycrystalline sample tested here. Testing this prediction experimentally would be another avenue for further study. Single crystal ClCuPc specimens could be studied to determine if the structural damage is truly reduced by encapsulation, and to what extent there is a reduction in mass loss.

Also worth further investigation is the 'latent dose' effect displayed by the encapsulated LiF. Experiments could be carried out, at different dose rates, to determine whether or not this phenomenon is due to a limited diffusion rate through the encapsulation layer. If that proves to be the case, then high-resolution microanalysis should be carried out at higher dose rates, rather than at lower ones.

Possibly the most significant suggestion for further work would be a study of the effect of the encapsulation layer's thickness on its protection factor. Fryer (1984) found no change in the structural protection factor, for encapsulation layers as thick as ~24 nm and as thin as ~8 nm. Since it is not known whether or not the same can be said for the reduction in mass loss, this deserves further investigation by EELS. In practice, the thinner the encapsulating layer, the less likely it is to interfere with microscopy of the radiation-sensitive material. So the question of just how thin an encapsulating layer can be,

before the protection factors are adversly effected, still remains to be answered. Such a study would require that each test specimen be prepared with a single-coated, and several (perhaps two) double-coated regions with encapsulating layer of different thickness.

It should also be mentioned that while the experiments discussed in section 4.4 did extend the list of materials on which encapsulation has been tested, the method is sufficiently new that many more radiation-sensitive materials remain to be tested. It would also be of interest to determine if the encapsulation's protection mechanism(s) functions at low temperatures. If encapsulation complemented the cryogenic method, the overall reduction in mass loss could be as high as 1000. Obviously a protection factor of that magnitude would allow high-resolution microanalysis of even highly-sensitive materials.

References

Berger, S.D. et al. (1987), Electron energy-loss spectroscopy studies of nanometre-scale structures in alumina produced by intense electron-beam irradiation, *Phil. Mag. B*, 55(3), p341-358.

Chadderton, L.T., Johnson, E., Wohlenberg, T. (1976), Observations of a Regular Void Array in Natural Fluorite Irradiated with 100 keV Electrons, *Physica Scripta*, 13, p127-128.

Cheng, S.C. (1987), Ph.D. Thesis, University of Alberta.

Clark, W.R.K., et al. (1980), Radiation Damage Mechanisms in Copper Phthalocyanine and its Chlorinated Derivatives, *Ultramicroscopy*, 5, p195-208.

Colliex, C. (1984), Electron Energy Loss Spectroscopy in the Electron Microscope, *Advances in Optical and Electron Microscopy*, eds. R. Barber and V.E. Cosslett, Academic Press, p65-177.

Disko, M.M. (1986), Practical Methods for Quantitative and Fine Structure Analysis of Energy Loss Spectra, *Microbeam Analysis--1986*, eds. A.D. Romig Jr. and W.F. Chambers, San Francisco Press, p429.

Egerton, R.F. (1978), Formulae for Light-Element Microanalysis by Electron Energy-Loss Spectrometry, *Ultramicroscopy* , 3, p243-251.

Egerton, R.F. (1979), K-shell Ionization Cross-Sections for use in Microanalysis, *Ultramicroscopy*, 4, p169-179.

Egerton, R.F. (1980a), Chemical Measurement of Radiation Damage in Organic Samples At and Below Room Temperature, *Ultramicroscopy*, 5, p221.

Egerton, R.F. (1980b), Instrumentation and Software for Energy-Loss Microanalysis, *Scanning Electron Microscopy*, 1980, part I, p41-52.

Egerton, R.F. (1981), The Range of Validity of EELS Microanalysis Formulae, *Ultramicroscopy*, 6, p297-300.

Egerton, R.F. (1982a), Principles and Practice of Quantitative Electron Energy-Loss Spectroscopy, *Microbeam Analysis--1982*, ed. K.F.J. Heinrich, San Francisco Press, p43-53.

Egerton, R.F. (1982b), Organic mass loss at 100K and 300K, *J. Microsc.* , 126(1), p95-100.

Egerton, R.F. (1986), *Electron Energy-Loss Spectroscopy in the Electron Microscope*, Plenum Press, New York.

Egerton, R.F. and Cheng, S.C. (1987), Measurement of Local Thickness By Electron Energy-Loss Spectroscopy, *Ultramicroscopy*, 21, p231-244.

Egerton, R.F., Crozier, P.A., Rice, P.M. (1987), EELS and Chemical Change, *Ultramicroscopy*, (in press).

Fryer, J.R. (1984), Radiation Damage in Organic Crystalline Films, *Ultramicroscopy*, 14, p227-236.

Fryer, J.R. and Holland, F.M. (1983), The Reduction of Radiation Damage in the Electron Microscope, *Ultramicroscopy*, 11, p67-70.

Gatan Instruction Manual

Hobbs, L.W. (1979), Radiation Damage in Electron Microscopy of Inorganic Solids, *Ultramicroscopy*, 3, p381-386.

Hobbs, L.W. (1983), Radiation Effects In Analysis By TEM, in *Quantitative Electron Microscopy*, eds. J.N. Chapman and A.J. Craven, Proceedings of the 25 Scottish Universities Summer School in Physics, p399-445.

Hobbs, L.W. (1984), Radiation Effects with Inorganic Specimens, in *Introduction to Analytical Electron Microscopy*, eds. J.J. Hren, J.I. Goldstein and D.C. Joy, Plenum Press, New York, p437-480.

Hobbs, L.W. and Pascucci, M.R. (1980), Radiolysis and defect structure in electron-irradiated α-quartz, *J. Physique*, Coll. C6, suppl. #7, 41, p237-242.

Inokuti, M. (1971), Inelastic collisions of fast charged particles with atoms and molecules - The Bethe theory revisited, *Rev. Mod. Phys.*, 43, p297-347

Isaacson, M. (1972), Interaction of 25 keV electrons with nucleic acid basis, adenine, thymine, and uracil.(II) Inner shell excitation and inelastic cross sections, *J. Chem. Phys.*, 56, p1812-1818.

Johnson, D.E. (1972), The interaction of 25 keV electrons with guanine and cytosine, *Radiat. Res.*, 49, p63-84.

Joy, D.C. (1984), Detectors For Electron Energy Spectroscopy, in *Electron Beam Interactions With Solids*, eds. D.F. Kyser, H. Niedrig, D.E. Newbury, and R. Shimizu, SEM Inc., 1984, p251-257.

Joy, D.C. and Maher, D.M. (1980), The Electron Energy-Loss Spectrum - Facts and Artefacts, *Scanning Electron Microscopy*, 1980, part I, p25-32.

Kabler, M.N. and Williams, R.T. (1978), Vacancy-interstitial pair production via electron-hole recombination in halide crystals, *Physical Review B*, 18(4), p1948-1960.

Leapman, R.D. (1982), EXELFS spectroscopy of amorphous materials, *Microbeam Analysis--1982*, Ed. K.F.J. Heinrich, San Francisco Press, p111-117.

Leapman, R.D., Grunes, L.A., and Fejes, P.L. (1982), Study of the $L_{2,3}$ edges in the 3d transition metals and their oxides by elctron energy-loss spectroscopy with comparisons to theory, *Phys. Rev. B*, 26, p614-635.

Maher, D., Mochel, P., and Joy, D.C. (1978), A data collection and reduction system for electron energy-loss spectroscopy, *Proc. 13 th Ann. Conf. Microbeam Analysis Soceity*, NBS Analytical Chemistry Division, Washington D.C., p53A-53K.

Mankiewich, P.M., et al. (1984), High resolution electron beam lithography on CaF_2, *Appl. Phys. Lett.*, 44(4), p468-469.

Mansfield, J.F., et al. (1987), Radiation Effects on X-Ray Microanalysis of a Light Element Alloy in a Medium-Voltage Electron Microscope, *Ultramicroscopy*, 21, p13-22.

Munoz, R. (1983), M. Sc. Thesis, University of Alberta.

Muray, A., et al. (1983), Fabrication of apertures, slots, and grooves at the 8-80 nm scale in silicon and metal films, *J. Vac. Sci. Technol. B*, 1(4), p1091-1095.

Muray, A., Isaacson, M., and Adesida, I. (1984), Fabrication of Nanometer Scale Structure, *Microbeam Analysis--1984*, eds. A.D. Romig Jr. and J.I. Goldstein, San Francisco Press, p70-71.

Salih, S.M. and Cosslett, V.E. (1974), Reduction in electron irradiation damage to organic compounds by conducting coatings, *Phil. Mag.*, 30, p225-228.

Smith, D.J., Fryer, J.R., Camps, R.A. (1986), Radiation Damage and Structural Studies: Halogenated Phthalocyanines, *Ultramicroscopy*, 19, p279-298.

Spence, J.C.H. (1980), *Experimental High-Resolution Electron Microscopy*, Oxford University Press, New York.

Szymonski, M. and de Vries, A.E. (1983), Sputtering of Alkali Halides by Electrons, in *Desorption Induced by Electronic Transitions (DIET 1)*, eds. N.H.Talk, M.M.Traum, J.C.Tally and T.E.Madey, Springer-Verlag, New York, p216.

Thomas, G. and Goringe, M.J. (1979), *Transmission Electron Microscopy of Materials*, John Wiley &Sons, New York.

Thomas, L.E. (1985), Light-Element Analysis with Electrons and X-Rays in a High-Resolution STEM, *Ultramicroscopy*, 18, p173-184.

Townsend, P.D. and Lama, F. (1983), The Contribution of Electronic Processes in Sputtering, in *Desorption Induced by Electronic Transitions (DIET 1)* , eds.,N.H.Talk, M.M.Traum, J.C.Tally and T.E.Madey, Springer-Verlag, New York, p220.

Uyeda, N., et al. (1972), Molecular image resolution in electron microscopy, *J. Appl. Phys.*, 43(12), p5181-5188.

Appendix A

Electron Diffraction

For crystal specimens in the electron microscope, Bragg scattering is responsible for the electron diffraction pattern (Thomas and Goringe 1979). Figure A.1 illustrates Bragg reflection for close-packed crystals ($\Theta \simeq 1°$). Consider the incident beam, of wavelength λ, as it strikes successive parallel planes of atoms (of interplanar spacing d) at an incident angle Θ. Some of the intensity is transmitted and some is reflected at an angle Θ to the planes. The diffracted waves (marked 1 and 2) will interfere constructively only if the path difference between the two waves is an integral multiple of the wavelength. For the situation displayed in figure A.1, the path difference (ab + bc) is equal to $2d\sin\Theta$. Hence, Bragg's law is

$$2d\sin\Theta = n\lambda$$

where n is the order of the reflection.

If the specimen is a single crystal, the diffraction pattern consists of a regular pattern of spots whose geometric design depends on the nature of the crystal and the direction of the the incident electrons. If the specimen is polycrystalline, however, the selective reflections form hollow cones, of semi angle Θ, which produce a pattern of concentric rings.

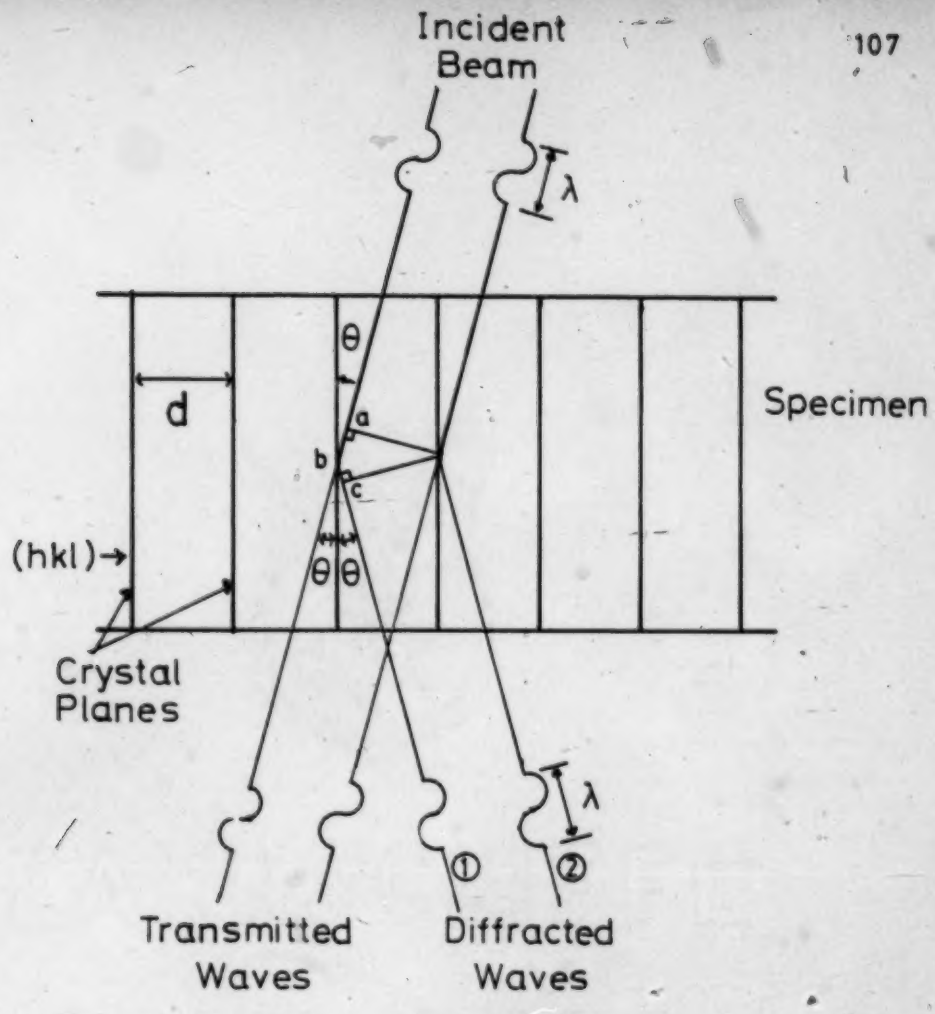

Fig A.1) Illustration of Bragg reflection for close-packed crystals.

In either case, the spots or rings can be indexed according to their Miller indices (hkl), which refer to the reflecting planes which gave rise to them. The reciprical lattice vector $\vec{g}$, whose magnitude is simply equal to the inverse of the interplanar spacing d, originates at the transmitted (unreflected) beam and ends at a reciprocal lattice point (hkl) on the reflecting (Ewald) sphere (a sphere or radius $1/\lambda$ in reciprocal space), as displayed in figure A.2.

When the microscope is in diffraction mode, the diffraction pattern is projected onto the fluorescent screen or onto a photographic plate. The microscope is thus said to have an effective camera length L. $\vec{R}_{hkl}$ is just the vector joining the transmitted spot to a particular diffraction spot (hkl) in the diffraction pattern (or in the case of polycrystalline samples, it is the radius of the (hkl) ring).

By using a standard specimen of known lattice constant (iron, for example), so that d can be calculated theoretically, it is possible to determine L. Starting with Bragg's law, and making the simplying assumption that $\sin\theta \simeq \tan\theta \simeq \theta$ (for $\theta \leq 17$mrad), it is possible to replace $\sin\theta$ with R/2L. Thus for n = unity, the equation becomes

$$\frac{d \cdot R}{L} = \lambda \ .$$

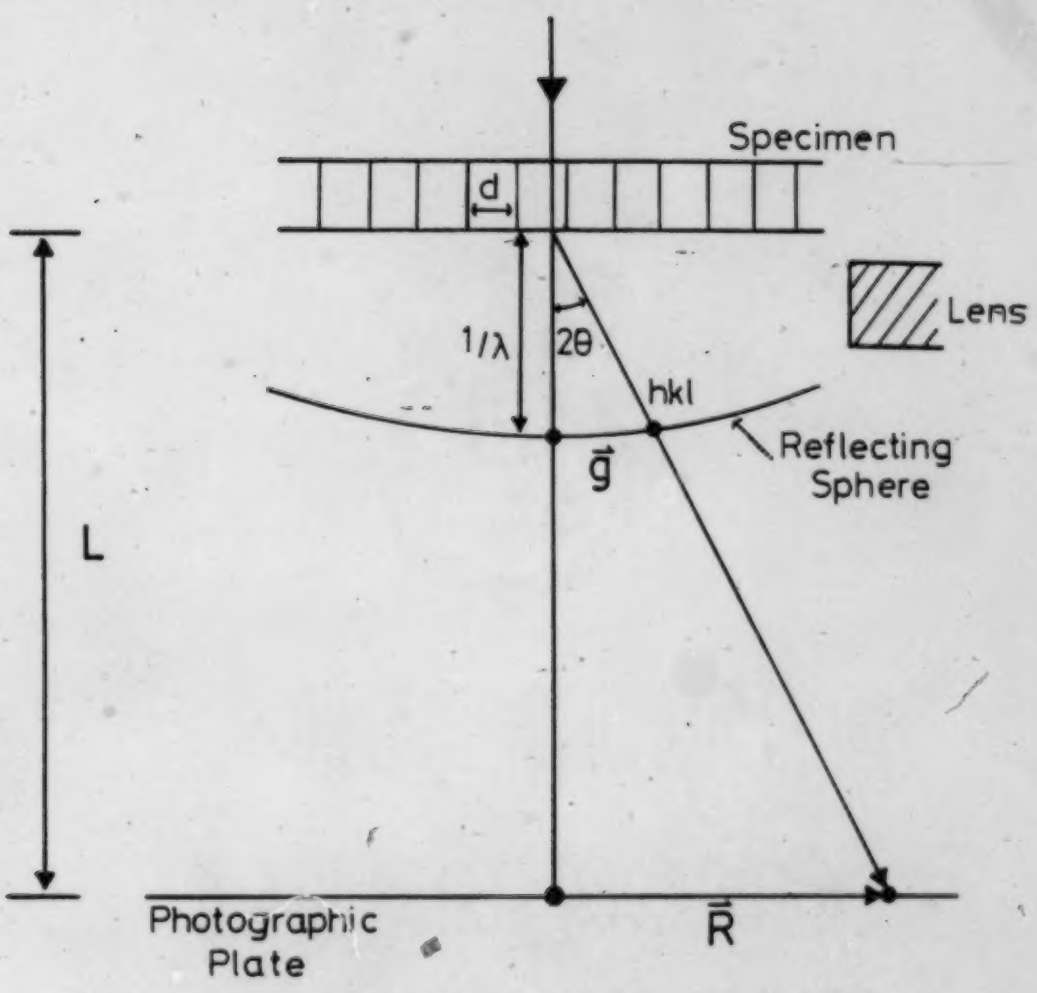

Fig A.2) Schematic diagram of the formation of a diffraction pattern in the transmission electron microscope, with effective camera length L.

In the case of an iron sample, $a/\sqrt{N}$ (where a=2.87 Å, the b.c.c. lattice parameter for Fe, and $N = h^2+k^2+l^2$) may be substituted for d. It is then possible to rewrite the equation as

$$R^2 = (\frac{L\lambda}{a})^2 N \ .$$

The R_{hkl} were measured from a photograph of the diffraction pattern, and the squares of their values were graphed as a function of N. The square root of the slope of the resultant line, multiplied by a/λ (for E_o = 80keV, λ=.0418 Å), gave the camera length to be L = 429mm.